Space–Time Wave Extremes: The Role of Metocean Forcings

FRANCESCO BARBARIOL, ALVISE BENETAZZO, SANDRO CARNIEL, AND MAURO SCLAVO

Institute of Marine Sciences (ISMAR)–Italian National Research Council (CNR), Venice, Italy

(Manuscript received 21 November 2014, in final form 10 March 2015)

ABSTRACT

Wave observations and modeling have recently demonstrated that wave extremes of short-crested seas are poorly predicted by statistics of time records. Indeed, the highest waves pertain to wave groups at focusing that have space–time dynamics. Therefore, the statistical prediction of extremes of short-crested sea states should rely on the multidimensional random wave fields' assumption. To adapt wave extreme statistics to the space–time domain, theoretical models using parameters of the directional wave spectrum have been recently developed. In this paper, the influence of metocean forcings (wind conditions, ambient current, and bottom depth) on these parameters and hence on wave extremes is studied with a twofold strategy. First, parametric spectral formulations [Pierson–Moskowitz and Joint North Sea Wave Project (JONSWAP) frequency spectra with $\cos^2$ directional distribution function] are considered to represent the dependence of wave extremes upon wind speed, fetch, and space domain size. Afterward, arbitrary conditions are simulated by using the SWAN numerical model adapted to store the spectral parameters, and the effects on extremes of current- and depth-induced shoaling are investigated. Preliminarily, the space–time extremes prediction model adopted is assessed by means of numerical simulations of Gaussian random seas. Compared to the significant wave height of the sea state and for a given space domain size, results show that space–time extremes are enhanced by opposite currents, whereas they are weakened by increasing wind conditions (wind speed and fetch) and by depth-induced shoaling. In this respect, the remarkable contribution to wave extremes of the size of the space domain is substantiated.

1. Introduction

During sea storms, marine structures and routing ships are exposed to severe wave conditions that are responsible for serious damages and occasional sinkings (Sand et al. 1990; Skourup et al. 1997; Socquet-Juglard 2005; Forristall 2007; Dysthe et al. 2008; Forristall 2011; Cavaleri et al. 2012). In this context, it is crucial for engineers, scientists, and seafarers to be able to predict the actual maximum sea surface elevation (or, equivalently, the maximum crest elevation or maximum wave height) a structure or a ship could encounter within a specific sea condition.

Traditionally, the sea surface elevation $\eta(x, y, t)$ (where x and y are the Cartesian space coordinates and t is the time) is retrieved recording the time series $\eta(t)$ by means of pointlike instruments (e.g., wave gauges, ultrasonic instruments, and buoys). In this context, the maximum expected wave height H and crest elevation C within a sea state have been defined by means of time extreme value analysis: $H_{\max} \approx 2.0H_s$ and $C_{\max} \approx 1.25H_s$ (where H_s is the significant wave height) have thus become rules of thumb for engineers and scientists (Dysthe et al. 2008). Although the probabilistic character of these estimates intrinsically accounts for the occurrence of even higher waves, occasionally the standard wave model framework based on the statistics of time records turned out to be poorly effective in describing extreme elevations, especially during short-crested sea states that are typical of storm conditions. Indeed, exceedances of the expected maximum crest heights as well as damages significantly above the corresponding level have been observed and a correct interpretation cannot be found even using second-order time wave statistics (Forristall 2005, 2006, 2007; Dysthe et al. 2008).

Recently, novel instrumentations [e.g., stereophotogrammetric systems (Shemdin et al. 1988; Banner et al. 1989) and radars (Dankert et al. 2003)] supported by increasing computing capabilities have allowed for the

Corresponding author address: Francesco Barbariol, Institute of Marine Sciences (ISMAR)–Italian National Research Council (CNR), Arsenale Tesa 104, Castello 2737/F, Venice 30122, Italy.
E-mail: francesco.barbariol@ve.ismar.cnr.it

DOI: 10.1175/JPO-D-14-0232.1

retrieval of 2D digital maps of the sea surface elevation $\eta(x, y)$ evolving over time. The change of the domain of observation from time to space–time revealed that during short-crested sea states the maximum sea surface elevation gathered over an area is larger than that obtained at a single fixed point inside the area. Indeed, Fedele et al. (2013) observed an increase of the maximum sea surface elevation with the area by means of a stereophotogrammetric system [namely, the Wave Acquisition Stereo System (WASS) (Benetazzo 2006; Benetazzo et al. 2012)] deployed on top of the oceanographic tower "Acqua Alta" in the northern Adriatic Sea (Italy). Socquet-Juglard et al. (2005) and Forristall (2005) verified the same evidence by numerical simulations of short-crested sea states, while Forristall (2011) observed this during a wave tank experiment. Besides these, the European project MaxWave concluded that extending the analysis to the space domain results in many more individual waves observed, and hence the standard model criteria for extreme waves have to be modified (Rosenthal and Lehner 2008). Indeed, the occurrence of larger waves in space–time is strictly related to an increase of the number of waves associated with a genuine dimensional effect (Baxevani and Rychlik 2006; Fedele 2012).

To interpret the observations of sea state maxima over space and time, theoretical models have been derived from the analysis of multidimensional random fields: the Piterbarg theorem (Piterbarg 1996) and Adler and Taylor's Euler characteristics approach (Adler 1981; Adler and Taylor 2007) have been applied to ocean wave statistics assuming that the sea surface $\eta(x, y, t)$ can be modeled as a Gaussian random surface over the 2D space (x, y) and the time t. These theories opened the door to space–time extreme value analysis, as they allow one to estimate the exceedance probability distribution functions (EDFs) and the expected values of extremes over space and time. Adaptations of space–time extreme theories to wave analysis, that is, the Piterbarg theorem (hereinafter PT) and the Fedele (2012) model (hereinafter FM) based upon Adler and Taylor's approach, have proved to be accurate in predicting synthetic (Forristall 2005, 2007; Krogstad et al. 2004; Socquet-Juglard et al. 2005), laboratory (Forristall 2011), and open sea maximum surface elevations over space–time (Fedele et al. 2013; Barbariol et al. 2014). Hence, these models could represent a change of paradigm in wave statistics and could support the explanation of the occurrence of extreme waves during storms, as demonstrated by Fedele (2012). Nevertheless, at present the diffusion of PT and FM is limited mainly because of the scarce availability of directional wave spectra, whose specific integral parameters are the inputs of space–time extreme models (Baxevani and Rychlik 2006; Fedele 2012).

Besides this, and most importantly, the coupling of such probabilistic models with the physical mechanisms suspected to be responsible for wave extremes' generation has not been investigated yet. The spatial focusing due to current-induced refraction, the dispersive focusing, and the nonlinear focusing, that is, the so-called Benjamin–Feir instability, have been proposed as the main factors that contribute to the genesis of extremely high waves (Dysthe et al. 2008). In agreement with the conclusions of the European project MaxWave (Rosenthal and Lehner 2008), which analyzed several marine accidents in order to improve the understanding of the physical processes of extreme waves generation, the influence of the metocean forcings on the space–time extremes should be assessed in order to detect the favorable conditions for extreme waves' occurrence. Indeed, the wind conditions (i.e., the wind speed and the fetch), the presence of an oceanic current, and the propagation onto a shallow-water environment intimately contribute to the sea state evolution and therefore could play a role in the generation of extreme waves. Such forcings directly affect the directional wave spectrum and, consequently, its integral parameters. Thus, analyzing how the spectral parameters are influenced by the metocean forcings provides an indirect assessment of the space–time extremes dependence upon them.

To this end, we propose two approaches aimed at computing the integral parameters of the directional spectrum required by the space–time extremes models, that is, the mean wave period τ, the components of the mean wavelength L_x and L_y, and the irregularity parameters α_{xt}, α_{xy}, and α_{yt}. The first approach is based upon the analytical integration of parametric directional wave spectra obtained by combining a deep-water frequency spectrum [i.e., Pierson–Moskowitz or Joint North Sea Wave Project (JONSWAP)] with the $\cos^2$ directional distribution function, representative of short-crested sea states. Two sets of formulas for the spectral parameters' computation in fully developed (i.e., Pierson–Moskowitz) or fetch-limited (i.e., JONSWAP) short-crested sea states are obtained and discussed. Their dependence upon wind speed and fetch is then used in order to assess the wind conditions' effect on the space–time extremes, which were estimated by means of FM. In addition, the space domain size effect on the space–time extremes is assessed. The second approach makes use of the numerical integration of directional spectra routinely performed by spectral numerical wave models over arbitrary computational domains. By taking the computation of the cited integral parameters into the model, the storage of the output spectra at each computational grid node and time step, which may be highly resource demanding, is avoided.

Therefore, version 40.85 of the Simulating Waves Nearshore (SWAN) model was adapted in order to develop an ad hoc version specifically suited to spectral parameters calculation that can be used in combination with theoretical space–time probabilistic models for wave extremes' prediction in arbitrary conditions. Then, the effects of current- and depth-induced shoaling on FM space–time extremes are studied using this model. Before discussing the dependence of space–time extremes upon metocean forcings, FM performance is assessed by means of numerical simulations of Gaussian random seas, as in Forristall (2006).

2. Space–time extremes of a sea state

A space–time (hereinafter ST) extreme of a sea state is defined as the maximum sea surface elevation within a given time duration T and over a specified sea surface area S (Krogstad et al. 2004; Fedele 2012), assuming the wave field stationary over time and homogeneous over space. If S is larger than the characteristic sizes of waves (say, the wavelength by the wave crest length), then an ST extreme most likely corresponds to the elevation of the highest crest of a 3D wave group at focusing (Fedele 2012). It is unlikely to attain the actual elevation of this crest at a fixed point of observation (i.e., by taking into account a time-dependent sea surface elevation), unless the sea state is long crested or the chosen point is located exactly where the crest apex occurs. Hence, in short-crested sea states, wave extremes should be observed by means of instruments spanning the ST domain (e.g., radars or stereophotogrammetric systems) and predicted as maxima of multidimensional random fields. This requires that the ST features of the sea state or the directional wave spectrum are known.

a. Space–time spectral parameters

The features of a sea state that are functional to ST extremes' prediction are specific integral parameters of the directional spectrum $S(\sigma, \theta)$ and stem from the spectral moments m_{ijl} defined as

$$m_{ijl} = \int_0^{2\pi} \int_0^{\infty} k_x^i k_y^j \sigma^l S(\sigma, \theta)\, d\sigma\, d\theta, \tag{1}$$

where σ is the radian relative frequency, and θ is the direction of propagation, such that $k_x = k\cos\theta$ and $k_y = k\sin\theta$ are the components of the wavenumber vector $\mathbf{k}$. According to Baxevani and Rychlik (2006) and Fedele (2012), these features, which will hereinafter be referred to as "spectral parameters", are the mean wave period τ, the mean wavelength components L_x and L_y in a Cartesian reference frame (x, y), and the irregularity parameters α_{xt}, α_{yt}, and α_{xy} expressed as

$$\tau = 2\pi\sqrt{\frac{m_{000}}{m_{002}}}, \quad L_x = 2\pi\sqrt{\frac{m_{000}}{m_{200}}}, \quad L_y = 2\pi\sqrt{\frac{m_{000}}{m_{020}}}$$
$$\alpha_{xt} = \frac{m_{101}}{\sqrt{m_{200}m_{002}}}, \quad \alpha_{yt} = \frac{m_{011}}{\sqrt{m_{020}m_{002}}}, \quad \alpha_{xy} = \frac{m_{110}}{\sqrt{m_{020}m_{200}}}. \tag{2}$$

The average number of "waves" over a ST domain depends upon the size of the domain (i.e., X, Y, and T) relative to the average size of the waves (i.e., τ, L_x, and L_y), corrected for the space–time correlation which is accounted for by α_{xt}, α_{yt}, and α_{xy}. In the time domain, the number of waves increases with T or in the presence of smaller wave periods τ. In the space domain, apart from larger S and a shorter wavelength, the number of waves increase also by taking shorter wave crest lengths, that is, the more the sea state is short crested. If the reference frame is chosen such that the x axis corresponds to the mean direction of wave propagation ($\bar{\theta}$), then L_x and L_y represent the mean wavelength and the mean wave crest length, respectively. In general, this orientation can be achieved through a rotation of the directional spectrum, which does not affect the estimate of the ST extremes. Under this assumption, the short crestedness is given by

$$\gamma_s = \sqrt{m_{020}/m_{200}} = L_x/L_y, \tag{3}$$

which approaches 0 in long-crested conditions and 1 in short-crested sea states (Baxevani et al. 2003). While the first set of parameters (i.e., τ, L_x, and L_y) accounts for the geometry of the ST domain, the latter (i.e., α_{xt}, α_{yt}, and α_{xy}) describes the kinematic properties of the sea state. In fact, according to Baxevani and Rychlik (2006), the irregularity parameters are defined as the ratio between the highest crests velocity (i.e., the velocity of the specular points) and the sea state drift velocity (i.e., the principal velocity). Besides, the irregularity parameters account for correlation between space and time (α_{xt}, α_{yt}) or space and space (α_{xy}) sea surface gradients. They can assume absolute values within 0 and 1 that correspond to the "confused" and "organized" sea state conditions, respectively, and influence the number of waves in the space–time domain. Indeed, the more the wave motion is organized, the smaller is the number of independent waves one has to expect in the space–time domain. For example, an organized sea with long-crested waves traveling toward the x direction has $\alpha_{xt} = 1$ and null α_{xy} and α_{yt}, whereas a confused sea with two wave systems traveling along the x

direction from opposite sides has all the parameters equal to zero. Therefore, as explained in section 2b, in the confused sea case the probability of encountering very large waves will be larger.

b. Expected extremes

Theoretical models that predict maxima of the Gaussian sea surface elevation $\eta(x, y, t)$ are PT and FM, which allow us to estimate the asymptotic EDFs of the sea state ST maxima and the expected values. The two models differ mainly on the treatment of the boundaries of the ST domain. In fact, PT assumes that maxima occur within the ST volume $V = XYT$ (where X is the size along the x axis, Y is the size along the y axis, and T is the sea state duration over time t). Hence, the domain must be large enough to contain the characteristic sizes of the waves, that is, $T \geq \tau$, $X \geq L_x$, and $Y \geq L_y$. On the contrary, FM assumes that the maxima can also occur on the boundaries of V, that is, on its faces and edges, implying that domain sizes can also be smaller than τ, L_x, and L_y. Therefore, in order to entail the widest range of conditions, we will consider FM for the rest of the study, aware that results obtained and the following considerations are partially shared with PT (Barbariol et al. 2014).

FM assumes that the ST extremes η_{ST} obey the following EDF:

$$P(\eta_{ST}/H_s \geq h) \simeq (16M_3h^2 + 4M_2h + M_1)\exp(-8h^2). \tag{4}$$

Here, M_3, M_2, and M_1 are the average numbers of waves within V, on its faces (i.e., XT, YT, and XY) and on its sides (i.e., X, Y, and T), respectively, and are defined as

$$\begin{aligned} M_3 &= 2\pi\frac{T}{\tau}\frac{X}{L_x}\frac{Y}{L_y}\sqrt{1-\alpha_{xt}^2-\alpha_{yt}^2-\alpha_{xy}^2+2\alpha_{xt}\alpha_{yt}\alpha_{xy}} \\ M_2 &= \sqrt{2\pi}\left(\frac{XT}{\tau L_x}\sqrt{1-\alpha_{xt}^2}+\frac{YT}{\tau L_y}\sqrt{1-\alpha_{yt}^2}\right. \\ &\quad \left.+\frac{XY}{L_xL_y}\sqrt{1-\alpha_{xy}^2}\right) \\ M_1 &= \frac{T}{\tau}+\frac{X}{L_x}+\frac{Y}{L_y} \end{aligned} \tag{5}$$

and depend upon the spectral parameters [Eq. (2)] and the ST domain size (i.e., X, Y, and T). The asymptotic limit of Eq. (4) provides the Gumbel-like distribution of maxima, whose expected value $E[\eta_{ST}] = \overline{\eta}_{ST}$ is given by (Fedele 2012)

$$\overline{\xi}_{ST} = \overline{\eta}_{ST}/H_s \simeq h_0 + \frac{\gamma_E}{16h_0 - \dfrac{(32M_3h_0 + 4M_2)}{(16M_3h_0^2 + 4M_2h_0 + M_1)}}. \tag{6}$$

In Eq. (6), h_0 is the mode of the asymptotic distribution and is obtained as the solution of $P(\eta_{ST}/H_s \geq h) = 1$; $\gamma_E \approx 0.5772$ is the Euler–Mascheroni constant; and $H_s \approx 4.004\sqrt{m_{000}}$. Hereinafter, "ST extreme" will refer to the expected value $\overline{\xi}_{ST}$ of Eq. (6), which holds for Gaussian sea states (as verified in section 5) and represents an approximation for realistic (non-Gaussian) sea states that exhibit higher crests due to nonlinearities.

The "dimension of the waves" with respect to the ST domain can be evaluated by means of the parameter β (Fedele 2012), expressed as

$$\beta = 3 - \frac{4M_2h_0 + 2M_1}{16M_3h_0^2 + 4M_2h_0 + M_1}, \tag{7}$$

which is a statistical indicator of the geometry of the space–time extremes $\overline{\xi}_{ST}$ within the volume ST. Parameter β ranges from 3 to 1, which corresponds to the limiting cases of fully 3D wave extremes occurring within the V and 1D extremes over a single (e.g., time) dimension, respectively. For β values ranging between 3 and 1, extremes are likely to occur also on the boundaries of the domain (i.e., faces and sides).

3. Parametric wave spectral formulations

In the context of sea states that depend solely on wind speed and fetch, the ST extremes $\overline{\xi}_{ST}$ can be attained from the spectral parameters [Eq. (2)] of directional spectra that are analytically integrable (directly or after some manipulations). In this study, such sea states are modeled by means of deep-water parametric wave spectral formulations. To this end, the directional spectrum $S(\sigma, \theta)$ is decomposed into the frequency spectrum $W(\sigma)$ and the directional distribution function $D(\theta)$ (assumed to be dependent on θ only), according to

$$S(\sigma, \theta) \simeq W(\sigma)D(\theta). \tag{8}$$

First, we consider the Pierson and Moskowitz (1964) variance density spectrum (hereinafter PM) that provides good fitting to fully developed sea states. PM is herein expressed as a function of the wind speed $U_{19.5}$ (19.5 m above the mean sea level) as

$$W_{PM}(\sigma) = Ag^2\sigma^{-5}e^{-B(g/U_{19.5}/\sigma)^4}, \tag{9}$$

where $A = 0.0081$ is the Phillips constant, $g \approx 9.81\,\mathrm{m\,s^{-2}}$ is the gravitational acceleration, and $B = 0.74$.

Younger and fetch-limited seas are modeled by means of the JONSWAP (hereinafter JON) spectrum (Hasselmann et al. 1973) that consists of a scaled PM (expressed in terms of $\sigma_p = 0.88g/U_{19.5}$) multiplied by a peak enhancement function (Holthuijsen 2007):

$$W_{\mathrm{JON}}(\sigma) = A_{\mathrm{JON}} g^2 \sigma^{-5} e^{-P(\sigma/\sigma_o)^{-4}} \gamma^{\exp\{-(1/2)[(\sigma/\sigma_o - 1)/\phi]^2\}} \tag{10}$$

with $P = 5/4$. Parameters A_{JON}, γ, σ_p, and ϕ provide the scaling of the spectrum, the peak enhancement, the position of the peak, and the width of the peak, respectively. It was found that the JON parameters' relationships with the wind speed U_{10} (10 m above mean sea level) and fetch F can be expressed in terms of power laws through the dimensionless peak frequency $\nu = (\sigma_p/2\pi)U_{10}/g$ and the dimensionless fetch $F^* = Fg/U_{10}^2$. We assume the power-law coefficients from Lewis and Allos (1990) to guarantee the transition to fully developed conditions as the sea state evolves (Young 1999): $A_{\mathrm{JON}} = 0.032\nu^{0.67}$, $\gamma = 5.87\nu^{0.86}$, and $F^* = 47.4\nu^{-3.03}$. Then, we express the JON parameters as power laws of F^*, which implicitly provides dependence of parameters upon U_{10} and F:

$$\begin{aligned} A_{\mathrm{JON}} &= 0.032(F^*/47.4)^{-0.67/3.03} = 0.045(F/U_{10}^2)^{-0.22} \\ \gamma &= 5.87(F^*/47.4)^{-0.86/3.03} = 9.18(F/U_{10}^2)^{-0.28} \\ \sigma_p &= 2\pi g/U_{10}(F^*/47.4)^{-1/3.03} = 103.66(FU_{10})^{-0.33}, \end{aligned} \tag{11}$$

with ϕ equal to the mean value 0.08, according to Gran (1992). Typically, $A_{\mathrm{JON}} \in [0.0081, 0.0032]$, $\gamma \in [1, 7]$ with a mean value of 3.3, and $\nu = (\sigma_p/2\pi)U_{10}/g \in [0.13, +\infty)$. For a constant U_{10}, Eq. (11) shows that spectral parameters decrease with increasing F, and they tend to the typical PM values as the sea state tends to fully developed conditions: $A_{\mathrm{JON}} \to A = 0.0081$, $\gamma \to 1$, and $\nu \to 0.13$.

To model the directional distribution of variance $D(\theta)$, we consider the $\cos^2$ function, which depends on the direction θ only (Holthuijsen 2007):

$$D(\theta) = \frac{2}{\pi}\cos(\theta - \overline{\theta})^2, \quad -\pi/2 \le (\theta - \overline{\theta}) \le \pi/2. \tag{12}$$

To further simplify the analyses, without loss of generality, we assume a mean wave direction $\overline{\theta} = 0$ rad, that is, propagation along the x axis of a Cartesian reference frame. In this context, L_x represents the mean wavelength, L_y is the mean wave crest length, and $\gamma_s \approx 0.58$. The directional spreading of $\cos^2$ is constant and equal to 31.5°, whereas it has been shown to be also frequency dependent in fetch-limited sea states (Ewans 1998). Nevertheless, we adopt the $\cos^2$ distribution to compute the space–time extremes in short-crested sea states, and we assess (section 6a) the error with respect to a more realistic directional spreading function [i.e., cos2s with (Ewans 1998) frequency-dependent parameterization of the spreading parameter s].

Directional spectra are finally obtained by combining one of the cited frequency spectra with the $\cos^2$ directional distribution function, in accordance with Eq. (8). Therefore, the PM-based directional spectrum (hereinafter called PM+$\cos^2$) is obtained from Eqs. (9) and (12), while the JON-based spectrum (hereinafter called JON+$\cos^2$) is obtained from Eqs. (10) and (12).

Spectral parameters [Eq. (2)] are obtained after calculation of the spectral moments [Eq. (1)]. In deep waters, according to the linear dispersion relationship, $\sigma^2 = gk$; therefore, $k_x = \sigma^2/g\cos(\theta)$, $k_y = \sigma^2/g\sin(\theta)$, and the spectral moments [Eq. (1)] can be rewritten in terms of σ only:

$$m_{ijl} = \int_0^{2\pi}\int_0^{\infty} \frac{\sigma^{2(i+j)+l}}{g^{i+j}} \cos^i(\theta)\sin^j(\theta) W(\sigma) D(\theta)\, d\sigma\, d\theta, \tag{13}$$

where the spectral decomposition [Eq. (8)] has been used to split the directional spectrum $S(\sigma, \theta)$ into $W(\sigma)$ and $D(\theta)$. Since the $\cos^2$ directional distribution function depends on θ only, Eq. (13) can be rearranged in order to separate the integrals:

$$m_{ijl} = \int_0^{2\pi} \cos^i(\theta)\sin^j(\theta) D(\theta)\, d\theta \int_0^{\infty} \frac{\sigma^{2(i+j)+l}}{g^{i+j}} W(\sigma)\, d\sigma. \tag{14}$$

Both the frequency spectra considered are proportional to σ^{-5} above the spectral peak. Then, when the exponent of σ in Eq. (14) is equal to 4, that is, $2(i + j) + l = 4$, the integral over σ is unbounded and spectral moments cannot be calculated (Ochi 2005). Given such spectral formulations, all the spectral parameters in Eq. (2), except τ, are affected by the nonintegrability of the second integral of Eq. (14). Thus, we limit the upper bound of integration over σ to a cutoff frequency σ_c. Since spectral parameters and ST extremes will depend to some extent on the choice of the cutoff frequency σ_c, we link σ_c to the physics of surface gravity waves, assuming it represents the higher frequency a harmonic wave of the spectrum could experience in the ordinary gravity waves range, that is, the gravity–capillary limit $\sigma_c = 60\,\mathrm{rad\,s^{-1}}$ (Holthuijsen 2007). A sensitivity analysis to assess the effect of the σ_c value on the ST extremes was conducted, and it is reported in section 3a.

a. PM+cos² spectral parameters formulae

Assuming $W(\sigma) = W_{\mathrm{PM}}(\sigma)$, according to Eqs. (9) and (12), Eq. (14) can be rewritten as

$$m_{ijl} = \frac{2}{\pi} A g^{2-(i+j)} \int_0^{2\pi} \cos^{i+2}(\theta) \sin^{j}(\theta)\, d\theta \times \int_0^{\sigma_c} \frac{\sigma^{2(i+j)+l}}{\sigma^5} e^{-B(g/U_{19.5}/\sigma)^4}\, d\sigma, \quad (15)$$

and it can be integrated to provide the moments of PM+cos^2:

$$\begin{aligned}
m_{000} &= \frac{A U_{19.5}^4}{4 g^2 B} \\
m_{002} &= \frac{A U_{19.5}^2 \sqrt{\pi}}{4\sqrt{B}} = \sqrt{\pi B} g^2 m_{000} U_{19.5}^{-2} \\
m_{020} &= \frac{A\Gamma(0,s)}{16} = \frac{B\Gamma(0,s) g^2}{4} m_{000} U_{19.5}^{-4} \\
m_{200} &= \frac{3A\Gamma(0,s)}{16} = \frac{3B\Gamma(0,s) g^2}{4} m_{000} U_{19.5}^{-4} \\
m_{101} &= \frac{2A\Gamma(1/4) U_{19.5}}{3\pi B^{1/4}} = \frac{8 B^{3/4} g^2 \Gamma(1/4)}{3\pi} m_{000} U_{19.5}^{-3} \\
m_{110} &= 0 \\
m_{011} &= 0, \quad (16)
\end{aligned}$$

where $\Gamma(1/4)$ and $\Gamma(0, s)$ are the Gamma and upper incomplete Gamma functions (Abramowitz and Stegun 1965), respectively, and $s = 1.296 \times 10^{-7} B(g/U_{19.5})^4$. The spectral parameters of PM+cos^2 are derived from Eqs. (16) and (2) as

$$\begin{aligned}
\tau &= \frac{2\pi^{3/4}}{g B^{1/4}} U_{19.5} \\
L_x &= a_1 \frac{\pi}{g\sqrt{B\Gamma(0,s)}} U_{19.5}^2 = \frac{4\pi}{g\sqrt{3B\Gamma(0,s)}} U_{19.5}^2 \\
L_y &= a_2 \frac{\pi}{g\sqrt{B\Gamma(0,s)}} U_{19.5}^2 = \frac{4\pi}{g\sqrt{B\Gamma(0,s)}} U_{19.5}^2 \\
\alpha_{xt} &= a_3 \frac{\Gamma(1/4)}{\sqrt{\pi^{5/2}\Gamma(0,s)}} = \frac{16\Gamma(1/4)}{3^{3/2}\pi\sqrt{\pi^{1/2}\Gamma(0,s)}} \\
\alpha_{yt} &= 0 \\
\alpha_{xy} &= 0. \quad (17)
\end{aligned}$$

Here, spectral parameters have been also shown in a general formulation using the coefficients a_1, a_2, and a_3 that depend on the power m of a general cos^m directional distribution function [i.e., accounting for $D_m(\theta) = N(m)\cos(\theta - \overline{\theta})^m$, with $N(m)$ a normalization coefficient depending on m]. In our context, if $m = 2$, then the coefficients assume the values shown in the rightmost part of Eq. (17): $a_1 = 4/\sqrt{3}$, $a_2 = 4$, and $a_3 = 16/(3^{3/2}\pi)$. Parameters L_x, L_y, and α_{xt} depend upon the maximum cutoff frequency σ_c through s. The function $\Gamma(0, s)$ can be calculated by using its upper limiting function $E_1(s) = -\gamma_E - \ln(s) - \sum_1^\infty (-s)^w/[w(w!)]$ (Abramowitz and Stegun 1965). In a wide range of wind speeds (i.e., from 1 to 40 m s^{-1}), we verified that the third term of $E_1(s)$ can be neglected, being eight orders of magnitude smaller than the first two terms. Therefore, by rearranging we obtain a simplified expression for $\Gamma(0, s)$, which is explicitly dependent upon $U_{19.5}$ and accurate to within a 10^{-5} root-mean-square error [RMSE = $(\{\sum_i [E_1(s_i) - \widetilde{E_1}(s_i)]^2\}/N)^{1/2}$, where $\widetilde{E_1}(s) = -\gamma_E - \ln s$]:

$$\Gamma(0,s) \approx 4(1.74 + \ln U_{19.5}). \quad (18)$$

It is noteworthy that the mean wave period τ is not a function of m or s, meaning that in this context and by definition it is independent of the directional spreading of the spectrum and the cutoff frequency. The expressions obtained for m_{000} and τ are consistent with results reported by Ochi (2005) for a spectral formulation with σ^{-5} tail. Besides, as $H_s = 2/g\sqrt{A/B}U_{19.5}^2$, the significant wave height is proportional to $U_{19.5}^2$, as indicated by Kitaigorodskii (1962) for a fully developed sea. The ratio $m_{200}/m_{020} = 3$ is independent of $U_{19.5}$. Consequently, the short crestedness associated with the cos^2 distribution ($\gamma_s = L_x/L_y \approx 0.58$) is recovered. In accordance with Baxevani and Rychlik (2006), the irregularity parameters are null, except for α_{xt}, which expresses the correlation between the sea surface derivatives over the direction of propagation x and the time t. Therefore, wave motion is somehow organized along x and a reduced number of exceedances of a certain threshold has to be expected inside the space–time domain and on its XT boundary. Instead, α_{xy} and α_{yt} equal zero since cos^2 is symmetric about $\overline{\theta}$.

To investigate the effects on the ST extremes of the cutoff frequency σ_c value, we performed a sensitivity analysis considered a PM+cos^2 with wind speed $U_{19.5} = 20$ m s^{-1}. The cutoff frequency $\sigma_c = 60$ rad s^{-1} was modified to 30 and 90 rad s^{-1} (i.e., 60 rad s^{-1} ±50%) and 12.56 rad s^{-1} (2.0 Hz). ST extremes $\overline{\xi}_{ST}$ were computed assuming a sea state duration $T = 100\tau$ and four different areas S ranging from 1 m^2 to 1000 × 1000 m^2. The variations with respect to the value associated with $\sigma_c = 60$ rad s^{-1}, expressed as $\Delta\overline{\xi}_{ST} = (\overline{\xi}_{ST_{\sigma_c}} - \overline{\xi}_{ST_{60}})/\overline{\xi}_{ST_{60}} \times 100$, are summarized in Table 1. The maximum absolute variation is 3.2% and occurs for $\sigma_c = 12.56$ rad s^{-1} and for $S = 100 \times 100$ m^2, that is, when area sides X and Y are of the same order of magnitude as L_x and L_y. Concerning the spectral parameters, the maximum absolute variation with respect to the values obtained with 60 rad s^{-1} is 24.8% (for L_x and L_y) again when $\sigma_c = 12.56$ rad s^{-1}. We conclude that while spectral parameters are moderately affected by σ_c, the ST extremes are only slightly sensitive to this choice. In this context, the results of the sensitivity analysis support the choice of the capillary–gravity limit as an appropriate cutoff frequency, since, besides the physical meaning, it represents a practical selection within a range of frequencies that assure a rather stable estimate of $\overline{\xi}_{ST}$.

TABLE 1. Effect of the cutoff frequency σ_c value on the ST extremes, expressed as the variation $\Delta\bar{\xi}_{ST}$ (%) with respect to the ST extremes associated with the capillary–gravity limit 60 rad s^{-1} (i.e., 9.5 Hz).

σ_c (rad s^{-1})	f_c (Hz)	$S = 1^2$ m^2	$S = 10^2$ m^2	$S = 100^2$ m^2	$S = 1000^2$ m^2
12.56	2.0	−0.5	−2.2	−3.2	−2.3
30.00	4.8	−0.1	−0.8	−1.1	−0.8
90.00	14.3	0.1	0.4	0.5	0.4

Finally, for a more practical computation of the spectral parameters of PM+cos^2, Eq. (17) can be rearranged accounting for Eq. (18), assuming the wind speed at 10-m elevation (i.e., $U_{10} \approx 0.93U_{19.5}$ within the near neutral conditions hypothesis) and taking the values of constants in place of symbols as

$$\begin{aligned}
\tau &\approx 0.56U_{10}\\
L_x &\approx \frac{0.50}{\sqrt{1.81+\ln U_{10}}}U_{10}^2\\
L_y &\approx \frac{0.86}{\sqrt{1.81+\ln U_{10}}}U_{10}^2\\
\alpha_{xt} &\approx \frac{1.34}{\sqrt{1.81+\ln U_{10}}}\\
\alpha_{yt} &= 0\\
\alpha_{xy} &= 0.
\end{aligned} \tag{19}$$

b. JON+cos^2 spectral parameters formulas

The procedure used to derive the PM+cos^2 spectral parameters cannot be applied to JON+cos^2, since $W_{JON}(\sigma)$ is not analytically integrable (Holthuijsen 2007). Therefore, spectral moments of JON+cos^2 have to be calculated in an approximate form. Yamaguchi (1984) obtained approximations for zeroth-, first-, and second-order moments of $W_{JON}(\sigma)$. Nonetheless, to compute the JON+cos^2 spectral moments up to the fourth order in frequency, we adopt the procedure used by Gran (1992) for JON and we adapt it to JON+cos^2. According to Gran (1992), $W_{JON}(\sigma)$ can be approximated by a peak-enhanced wave spectrum consisting of two independent components: (i) a broadbanded component conforming to a PM spectrum with $A = A_{JON}$ and peak frequency σ_p (responsible for the low- and high-frequency tails of the spectrum) and (ii) a narrowbanded component (hereinafter NB) with density closely centered about σ_p. Moments of JON+cos^2 are therefore obtained as the sum of the two contributions:

$$m_{ijl} \approx m_{ijl,PM} + m_{ijl,NB}, \tag{20}$$

where $m_{ijl,PM}$ are the moments of PM+cos^2, and $m_{ijl,NB}$ are the moments of the additional peak that are expressed in terms of a parameter δ, which Gran (1992) estimated to be

$$\delta = \frac{m_{000,NB}}{m_{000,PM}} \approx \frac{\gamma-1}{6}, \tag{21}$$

assuming $\phi = 0.08$ in Eq. (10). Parameter δ depends upon the peak enhancement factor γ, such that if $\gamma = 1$ then $\delta = 0$ and if $\gamma = 7$ then $\delta = 1$. Thus, using Eq. (21), $m_{ijl,NB}$ can be written as

$$m_{ijl,NB} = \delta\frac{\sigma_p^{2(i+j)+l}}{g^{(i+j)}}m_{000,PM}\int_0^{2\pi}\cos^i(\theta)\sin^j(\theta)D(\theta)\,d\theta. \tag{22}$$

Analytic integration of Eq. (22) leads to the moments of NB:

$$\begin{aligned}
m_{000,NB} &= \delta\frac{A_{JON}g^2}{4P\sigma_p^4}\\
m_{002,NB} &= \delta\frac{A_{JON}g^2}{4P\sigma_p^2}\\
m_{020,NB} &= \delta\frac{A_{JON}}{16P}\\
m_{200,NB} &= \delta\frac{3A_{JON}}{16P}\\
m_{101,NB} &= \delta\frac{2A_{JON}g}{3\pi P\sigma}\\
m_{110,NB} &= 0\\
m_{011,NB} &= 0.
\end{aligned} \tag{23}$$

Hence, according to Eq. (20), the moments of JON+cos^2 are

$$\begin{aligned}
m_{000} &\approx (\delta+1)\frac{A_{JON}g^2}{4P\sigma_p^4} = (\delta+1)m_{000,PM}\\
m_{002} &\approx (\delta+\sqrt{\pi P})\frac{A_{JON}g^2}{4P\sigma_p^2} = (\delta+\sqrt{\pi P})m_{000,PM}\sigma_p^2\\
m_{020} &\approx [\delta+P\Gamma(0,z)]\frac{A_{JON}}{16P} = \left[\frac{\delta+P\Gamma(0,z)}{4g^2}\right]m_{000,PM}\sigma_p^4\\
m_{200} &\approx [\delta+P\Gamma(0,z)]\frac{3A_{JON}}{16P} = 3\left[\frac{\delta+P\Gamma(0,z)}{4g^2}\right]m_{000,PM}\sigma_p^4\\
m_{101} &\approx [\delta+P^{3/4}\Gamma(1/4)]\frac{2gA_{JON}}{3\pi P\sigma_p}\\
&= \frac{8}{3\pi g}[\delta+P^{3/4}\Gamma(1/4)]m_{000,PM}\sigma_p^3\\
m_{110} &= 0\\
m_{011} &= 0,
\end{aligned} \tag{24}$$

where $m_{000,\mathrm{PM}} = A_{\mathrm{JON}} g^2/(4P\sigma_p^4)$ is the total variance associated with the broadbanded component, which results from Eq. (16) by taking $A = A_{\mathrm{JON}}$ and $U_{19.5} = 0.88g/\sigma_p$. Here, $\Gamma(0, z)$ is the upper incomplete Gamma function and $z = 1.296 \times 10^{-7} P\sigma_p^4$. The significant wave height of JON+cos^2, after Eqs. (24) and (21), is $H_s = 2g\sqrt{(\gamma+5)A/6/P}\sigma_p^{-2}$. Finally, the JON+cos^2 spectral parameters are obtained from Eqs. (2) and (24), through Eq. (21):

$$
\begin{aligned}
\tau &\approx \frac{2\pi}{\sigma_p}\sqrt{\frac{\gamma+b_1}{\gamma+(b_2\sqrt{\pi P}-1)}} = \frac{2\pi}{\sigma_p}\sqrt{\frac{\gamma+5.0}{\gamma+(6\sqrt{\pi P}-1)}}\\
L_x &\approx a_1\frac{\pi g}{\sigma_p^2}\sqrt{\frac{\gamma+b_1}{\gamma+b_2 P\Gamma(0,z)-1}} = \frac{4\pi g}{\sqrt{3}\sigma_p^2}\sqrt{\frac{\gamma+5.0}{\gamma+6P\Gamma(0,z)-1}}\\
L_y &\approx a_2\frac{\pi g}{\sigma_p^2}\sqrt{\frac{\gamma+b_1}{\gamma+b_2 P\Gamma(0,z)-1}} = \frac{4\pi g}{\sigma_p^2}\sqrt{\frac{\gamma+5.0}{\gamma+6P\Gamma(0,z)-1}}\\
\alpha_{xt} &\approx a_3\frac{[\gamma+b_2P^{3/4}\Gamma(1/4)-1]}{\sqrt{\gamma+b_2\sqrt{\pi P}-1}\sqrt{\gamma+b_2P\Gamma(0,z)-1}} = \frac{16[\gamma+6P^{3/4}\Gamma(1/4)-1]}{3^{3/2}\pi\sqrt{\gamma+(6\sqrt{\pi P}-1)}\sqrt{\gamma+6P\Gamma(0,z)-1}}\\
\alpha_{yt} &= 0\\
\alpha_{xy} &= 0.
\end{aligned}
\tag{25}
$$

Here, as for PM+cos^2, parameters are also shown in a general formulation where coefficients b_1 and b_2 add to the coefficients a_1, a_2, and a_3 obtained for PM+cos^2. They all depend upon the power m of $D_m(\theta)$. For the specific case considered (i.e., $m = 2$), $b_1 = 5$ and $b_2 = 6$. Once again, the parameters L_x, L_y, and α_{xt} depend upon the cutoff frequency through z, that is, the argument of the upper incomplete Gamma function. A simplified expression for $\Gamma(0, z)$, which is explicitly dependent upon σ_p and accurate within a 10^{-5} order RMSE is

$$
\Gamma(0,z) \approx 4(3.89 - \ln\sigma_p). \tag{26}
$$

Similar to what was obtained for PM+cos^2, the ratio m_{200}/m_{020} is independent of σ_p and $\gamma_s \approx 0.58$. Besides, since we chose formulations of the JON parameters of Eq. (11) that account for the transition to fully developed conditions, if $\delta = 0$ (i.e., $\gamma = 1$), then the PM+cos^2 parameters of Eq. (17) are recovered (taking $\sigma_p = 0.88g/U_{19.5}$). The dependence of spectral parameters upon U_{10} and F was intentionally not achieved in Eq. (25) in order to provide equations that are as compact as possible. However, it can be easily obtained by using the parameterizations for γ and σ_p provided by Eq. (11).

Though derived analytically, Eq. (25) benefits from the approximation of Gran (1992) for the JON spectrum, and hence it is not exact. Thus, we estimated the error introduced in the computation of spectral parameters by such an approximation. To this end, we compared the moments and parameters computed analytically by means of Eqs. (17) and (25) with those computed numerically (i.e., after the numerical integration of a discrete spectrum, accounting for a high-frequency tail proportional to σ^{-5}). We assumed the numerical estimates as benchmarks since we verified that for a PM+cos^2 spectrum (whose spectral parameter formulas are exact) the analytical and numerical estimates were exact within a few per thousand difference, which is the error introduced by the numerical integration technique. For JON+cos^2, in the range of γ between 1 and 7, we obtained differences between numerical and analytical results within 5% for spectral parameters of Eq. (2) and the significant wave height, H_s being the most affected parameter, since the JON approximation mostly affects the zeroth moment (i.e., m_{000}). Hence, thanks to the results of the sensitivity analysis on σ_c (section 3a), we expect much smaller errors on ST extremes.

Finally, accounting for Eq. (26) and taking the values of constants in place of symbols, Eq. (25) can be rearranged for a practical use of JON+cos^2 spectral parameters as

$$
\begin{aligned}
\tau &\approx \frac{6.3}{\sigma_p}\sqrt{\frac{\gamma+5.0}{\gamma+10.9}}\\
L_x &\approx \frac{71.2}{\sigma_p^2}\sqrt{\frac{\gamma+5.0}{\gamma-30.0\ln\sigma_p+115.7}}\\
L_y &\approx \frac{123.3}{\sigma_p^2}\sqrt{\frac{\gamma+5.0}{\gamma-30.0\ln\sigma_p+115.7}}\\
\alpha_{xt} &\approx \frac{\gamma+24.7}{\sqrt{\gamma+10.9}\sqrt{\gamma-30.0\ln\sigma_p+115.7}}\\
\alpha_{yt} &= 0\\
\alpha_{xy} &= 0.
\end{aligned}
\tag{27}
$$

4. Numerical modeling

The numerical integration of arbitrary directional spectra, that is, in deep to shallow waters and accounting for generation, propagation, and dissipation processes, is routinely performed with spectral numerical wave models. In this context, we adapted the SWAN model (version 40.85) in order to calculate the integral parameters [Eq. (2)] of the directional wave spectrum as output variables, and we hereinafter call this implementation SWAN-ST. With this implementation, the storage of the output spectra at each computational grid node and time step, which may be highly demanding of resources, is avoided.

a. The SWAN model

SWAN is a third-generation spectral wave model that simulates the generation, evolution, and dissipation of the directional wave spectrum $S(\sigma, \theta)$ at each node of a computational domain by numerically solving the wave action density equation (Booij et al. 1999):

$$\frac{\partial A(\sigma,\theta)}{\partial t}+\frac{\partial c_{g,x}A(\sigma,\theta)}{\partial x}+\frac{\partial c_{g,y}A(\sigma,\theta)}{\partial y}+\frac{\partial c_{g,\theta}A(\sigma,\theta)}{\partial \theta}+\frac{\partial c_{g,\sigma}A(\sigma,\theta)}{\partial \sigma}=\frac{F(\sigma,\theta)}{\sigma}. \quad (28)$$

Here, $A(\sigma, \theta) = \rho g S(\sigma, \theta)/\sigma$ is the wave action variance density spectrum and ρ is the water density. Equation (28) is a radiative, time-dependent transport equation that accounts for the wind input, the wave–wave interactions, and the dissipation phenomena both in deep and shallow waters. Processes characterizing wave propagation, such as shoaling, refraction, and wave–current interaction, are represented in the left-hand side of Eq. (28), while wind input, wave–wave interactions, and dissipations are included in the right-hand side of Eq. (28), that is, in the source term $F(\sigma, \theta)$. To model the processes included in the source term of Eq. (28), SWAN adopts the Wave Model (WAM) cycle III (Hasselmann et al. 1988) and WAM cycle IV (Günther et al. 1992) formulations (SWAN Team 2011). In addition, SWAN includes depth-induced breaking, bottom friction, and triad wave–wave interactions in intermediate/shallow waters. In SWAN, the physical and spectral spaces are discretized; direction θ is represented by N bins θ_n ($n = 1, \ldots, N$), divided by a constant step $\Delta\theta$, while frequencies are geometrically distributed in the prognostic range according to $\sigma_{i+1} = 1.1\sigma_i$ between σ_1 and σ_Q, that is, the minimum and maximum cutoff frequencies, respectively. Spectral moments of the spectrum are computed by adding a diagnostic tail proportional to σ^{-r} beyond σ_Q. Usually, r equals 4 or 5, but $r = 5$ is often preferred to resemble observed spectral tails (Pierson and Moskowitz 1964; Hasselmann et al. 1973; Forristall 1981).

b. The SWAN-ST implementation

We provided SWAN with new routines to obtain the parameters of the directional spectrum [Eq. (2)] as model outputs at each node of the physical domain (x, y) and each time step. In accordance to what is routinely done by SWAN, the frequency domain is subdivided into prognostic (P) and diagnostic (D) ranges. Therefore, spectral moments are split into two contributions, such that $m_{ijl} = m_{ijl,P} + m_{ijl,D}$. In the prognostic range of frequencies ($\sigma_1 \le \sigma_q \le \sigma_Q$), the spectrum is numerically integrated to compute spectral moments according to

$$m_{ijl,P} \approx \lambda \sum_{n=1}^{N}\sum_{q=1}^{Q} k_q^{(i+j)} \cos^i(\theta_n)\sin^j(\theta_n)\sigma_q^{(2+l)}A(\sigma_q,\theta_n)\Delta\theta, \quad (29)$$

where $\lambda = \ln(\sigma_{i+1}/\sigma_i)$. In the diagnostic range of frequencies ($\sigma_Q < \sigma < \infty$), the wave spectrum is analytically integrated in a way that

$$m_{ijl,D} \approx \tau[k_Q^{(i+j)} \cos^i(\theta_N)\sin^j(\theta_N)\sigma_Q^{(2+l)}A(\sigma_Q,\theta_N)\Delta\theta] \quad (30)$$

where $\tau = 1/\{\chi[1 + \chi(\upsilon - 1)]\}$, $\chi = r - l - 2(i + j) - 1$, and $\upsilon = \sqrt{\sigma_{i+1}/\sigma_i}$. Since the high-frequency tail is chosen as proportional to σ^{-5} when $2(i + j) + l \neq 4$, then χ vanishes and $m_{ijl,D}$ tends to be unbounded. Therefore, moments m_{200}, m_{020}, and m_{101} are obtained by integrating up to a maximum cutoff frequency $\sigma_c > \sigma_Q$:

$$m_{ijl,D} \approx m_{ijl,Dc} = \kappa[k_Q^{(i+j)} \cos^i\theta_N \sin^j\theta_N \sigma_Q^{(2+l)}A(\sigma_Q,\theta_N)\Delta\theta], \quad (31)$$

where $\kappa = \ln(\sigma_c) - \ln(\upsilon\sigma_Q)$. The choice of σ_c is arbitrary since the chosen value can be directly put into Eq. (31). In this study, we imposed σ_c equal to the gravity–capillary limit, that is, $\sigma_c = 60\,\mathrm{rad\,s^{-1}}$, for the reasons reported in section 3.

Equations (29)–(31) were implemented into the SWAN source code. To this end, two subroutines were written: one aimed at computing the spectral moments as described above and one aimed at computing the spectral parameters according to Eq. (2). In addition, the original source code was adapted in order to include the new subroutines and to allow the computation of five additional output variables: L_x, L_y, α_{xt}, α_{yt}, and α_{xy} (τ corresponds to the SWAN output variable $T02$). The subroutines and modules that were modified are those in charge of output variables' initialization and output requests' processing.

To validate the SWAN-ST implementation, a regression test was performed by first simulating the propagation of a PM+cos^2 directional spectrum with SWAN-ST and then by comparing the spectral parameters computed by the model with the spectral parameters analytically obtained from Eq. (19). In fact, we expected a correspondence of the two sets of parameters within some differences introduced by the model numerics. To this end, we simulated the stationary 1D propagation of a PM+cos^2 directional spectrum with $H_s = 4$ m imposed as boundary condition at the first node of a computational domain 500 km long with a 1-km resolution grid. The prognostic frequency range, consisting of 32 geometrically distributed frequencies, spans within 0.31 and 3.14 rad s^{-1} (i.e., from 0.05 to 1.00 Hz). Directions were discretized using 180 equally spaced values within the full circle $[0, 2\pi)$ rad. To consistently compare the spectral parameters obtained from Eq. (19), without loss of generality, we imposed peak direction $\theta_p = 0$ rad, which corresponds to the x-axis direction ($\overline{\theta} = \theta_p$ since PM+cos^2 is symmetric). No source term was included, since we were only interested in the propagative terms of Eq. (28). From the comparison between analytical and numerical results emerged that differences were smaller than 1% for all the spectral parameters. Thus, we concluded that the SWAN-ST implementation provides reliable estimates of the spectral parameters of Eq. (2).

Since most of the sea state energy/variance content is generally represented within the prognostic range of the wave spectrum, we also assessed the contribution of the diagnostic tail to the ST extremes $\overline{\xi}_{\mathrm{ST}}$. In fact, it was proven that the highest-frequency components of the spectral tail produce small ripples on the surface of high waves, without affecting the crest, trough, and wave heights significantly (Boccotti 2000). A sensitivity analysis was therefore conducted by comparing the ST extremes obtained accounting only for the prognostic frequency range of the spectrum with those obtained accounting for the whole prognostic and diagnostic range. Practically, parameters in the prognostic range were computed by means of the moments in Eq. (29), while parameters in the whole range were computed by adding to Eq. (29) either the moments in Eq. (30) or the moments in Eq. (31), assuming $\sigma_c = 60$ rad s^{-1}. We adopted the same physical and spectral discretization used for the regression test as well as the same general setup (i.e., stationary 1D propagation without source terms). However, in order to evaluate the effect of the peak to maximum cutoff frequency ratio (σ_p/σ_Q, where $\sigma_Q = 3.14$ rad s^{-1}), we accounted for four different sea states with $H_s = 1.0$, 2.0, 4.0, and 8.0 m, pointing out that $\sigma_p = 0.4\sqrt{g/H_s}$ for PM. We tested four different sizes of the space domain S: 1×1 m^2, 10×10 m^2, 100×100 m^2, and 1000×1000 m^2 (time domain extension T was constant and equal to 1800 s). The results are presented in Table 2 in terms of variations $\Delta\overline{\xi}_{\mathrm{ST}} = (\overline{\xi}_{\mathrm{ST}_{NT}} - \overline{\xi}_{\mathrm{ST}_T})/\overline{\xi}_{\mathrm{ST}_T} \times 100$: that is, with (subscript T) and without (subscript NT) the spectral tail.

TABLE 2. Effect of the spectral tail contribution on the ST extremes estimate, expressed as the variation $\Delta\overline{\xi}_{\mathrm{ST}}$ (%), that is, with and without the spectral tail.

H_s (m)	σ_p/σ_Q	$S = 1^2$ m^2	$S = 10^2$ m^2	$S = 100^2$ m^2	$S = 1000^2$ m^2
1.0	0.20	−2.9	−5.7	−4.6	−3.5
2.0	0.14	−1.7	−4.9	−4.4	−3.2
4.0	0.10	−0.9	−3.9	−4.2	−3.1
8.0	0.07	−0.5	−2.7	−4.1	−3.0

We note in Table 2 that $\Delta\overline{\xi}_{\mathrm{ST}}$ are always negative, meaning that neglecting the tail contribution leads to lower $\overline{\xi}_{\mathrm{ST}}$. For each H_s, the maximum absolute $\Delta\overline{\xi}_{\mathrm{ST}}$ is obtained when S is in the same order of magnitude as L_xL_y, while the global absolute maximum is 5.7%, which points out that, in the tested ranges of S and H_s, the ST extremes are only slightly sensitive to the tail contribution, consistent with the Boccotti's results. Additionally, differences are smaller for the highest sea states. In fact, $\Delta\overline{\xi}_{\mathrm{ST}}$ diminishes for decreasing σ_p/σ_Q, which is reasonable since higher sea states are associated with lower σ_p, and hence the prognostic range encompasses the most of the spectral variance, more than what happens for lower sea states. Furthermore, the largest areas (i.e., 100×100 m^2 and 1000×1000 m^2) show the lowest variabilities over H_s. This can be explained by the means of the wave dimension β; indeed for large areas, $\beta \simeq 3$, and it seems to be unaffected by the tail contribution and by the significant wave height. Besides this, results of this sensitivity analysis allowed us to estimate which is the effect of neglecting the spectral tail, which is a reasonable choice when its shape is unknown or is not correctly represented by the available parameterizations.

5. Assessment of FM predictions

Preliminarily, ST extremes predicted by FM were compared to the ST extremes obtained from numerical simulations of Gaussian random seas with PM+cos^2 and JON+cos^2 directional spectra. This approach was used among the others by Forristall (2006) to show the agreement between simulated and predicted (according to PT) ST extremes. To generate a large number of realizations of the Gaussian process $\eta(x, y, t)$ from a prescribed directional spectrum, we employed the Wave Analysis for Fatigue and Oceanography (WAFO) toolbox (WAFO Group 2011) for MATLAB, which has already been applied for simulations of wave extremes

TABLE 3. Assessment of FM model performance for two Gaussian sea states (PM+cos^2 and JON+cos^2) through the comparison of simulated (given with standard deviation) and predicted $\overline{\eta}_{ST}$ (m).

	$S = 1^2 L_x L_y\,\mathrm{m}^2$	$S = 2^2 L_x L_y\,\mathrm{m}^2$	$S = 3^2 L_x L_y\,\mathrm{m}^2$	$S = 4^2 L_x L_y\,\mathrm{m}^2$	$S = 5^2 L_x L_y\,\mathrm{m}^2$
PM+cos^2					
Simulated	1.24 ± 0.08	1.32 ± 0.07	1.35 ± 0.06	1.38 ± 0.06	1.40 ± 0.06
Predicted	1.23	1.30	1.34	1.37	1.39
JON+cos^2					
Simulated	1.24 ± 0.07	1.31 ± 0.07	1.36 ± 0.07	1.40 ± 0.07	1.42 ± 0.07
Predicted	1.25	1.31	1.35	1.38	1.40

(e.g., Gemmrich and Garrett 2008). Hence, a PM spectrum and a JON spectrum were alternatively combined with the cos^2 directional distribution to simulate a fully developed sea state and a fetch-limited sea state, respectively. The frequency spectra were imposed in order to simulate sea states with $H_s = 1.0$ m, $L_x \approx 14$ m, and $L_y \approx 14$ m. The frequency–direction domain was discretized using 7200 equally spaced frequencies between 2.8×10^{-4} (i.e., the frequency resolution) and 2 Hz and 180 directions with 2° resolution. For each sea state, we generated 100 independent realizations of $\eta(x, y, t)$, with spatial resolutions $\Delta x = \Delta y = 0.5$ m and temporal resolution $\Delta t = 0.25$ s. Then, from each realization we extracted the maxima η_{ST} over five ST volumes V_j ($j = 1, 2, 3, 4, 5$) with the same duration $T = 1$ hour and different areas $S_j = j^2 L_x L_y$. In Table 3, the expected extremes $\overline{\eta}_{ST}$ from numerical simulations are compared to the theoretical predictions of FM.

The numerical simulations provided $\overline{\eta}_{ST}$ ranging between 1.24 and 1.42 m, with coefficients of variation (standard deviation to expected value ratio) below 7%. The theoretical predictions of FM gave $\overline{\eta}_{ST}$ ranging from 1.23 to 1.40 m. In this context, the discrepancy between theoretical FM extremes and simulated expected extremes $[(\overline{\eta}_{ST_{FM}} - \overline{\eta}_{ST_{sim}})/\overline{\eta}_{ST_{sim}} \times 100]$ is smaller than 1.5% (in magnitude). We did not observe a significant trend of the error with respect to the area size nor a better performance with one sea state or the other. Therefore, even if we limited the significant wave height and the area of the domain in order to contain the computational effort, results in Table 3 point out an excellent agreement between simulated and predicted ST extremes for all the areas taken into account. Moreover, the FM performance is also remarkable if ST predictions are compared to the expected extremes at a point from standard Gaussian time statistics (i.e., Rayleigh), which are 0.97 (PM+cos^2) and 0.98 m (JON+cos^2).

6. Results

To evaluate metocean forcings' effects on ST extremes, analyses were conducted by the means of the analytical formulation and the numerical implementation of the spectral parameters discussed in sections 3 and 4. In particular, equations of the PM+cos^2 and JON+cos^2 spectral parameters were used to investigate the dependence upon the wind speed and fetch. In addition, in order to assess the spatial effect on ST extremes, the dependence of the space domain size was investigated. Afterward, the SWAN-ST implementation was employed to study the effects of current- and depth-induced shoaling.

a. *Wind speed and fetch effects*

The ST extremes $\overline{\xi}_{ST}$ were computed by feeding Eq. (6) with the spectral parameters obtained from Eqs. (19) and (27). The ranges of wind speed ($U = U_{10}$) and fetch F were chosen such that U varied within 10 and 20 m s^{-1} [i.e., approximately the Pierson and Moskowitz (1964) experimental range], while F varied from 1 to 250 km. Thus, only the frequency part of the considered spectra was interested by the wind variability, whereas the cos^2 distribution remained unchanged. Doing so, we achieved ST extremes of single independent sea states undergoing different wind conditions. The space domain size S varied from 1 to 10^6 m^2 in order to span a wide range of sea areas and assume the hypothesis of homogeneity was reasonably fulfilled. Focusing on the spatial contribution to $\overline{\xi}_{ST}$ rather than on the temporal contribution, the duration of the sea states was fixed, imposing $T = 100\tau$ in order to maintain a constant number of waves over the time domain while changing wind conditions [100 wave periods being a reasonable number to achieve meaningful statistical properties and stationarity of the sea states (Boccotti 2000; Holthuijsen 2007)].

The ST extremes $\overline{\xi}_{ST}(U, S)$ for PM+cos^2 and the ST extremes $\overline{\xi}_{ST}(U, F, S)$ for JON+cos^2 are shown in Figs. 1 and 2, respectively. In fully developed conditions (Fig. 1), $\overline{\xi}_{ST}(U, S)$ ranges from 0.8 to 1.5, growing for increasing S and reducing for increasing U. The dependence upon U seems weaker than that upon S; indeed, the whole range of the $\overline{\xi}_{ST}(U, S)$ variability is covered by modifying S for a given U, while modifying U for a given S, the maximum $\overline{\xi}_{ST}(U, S)$ variation is only

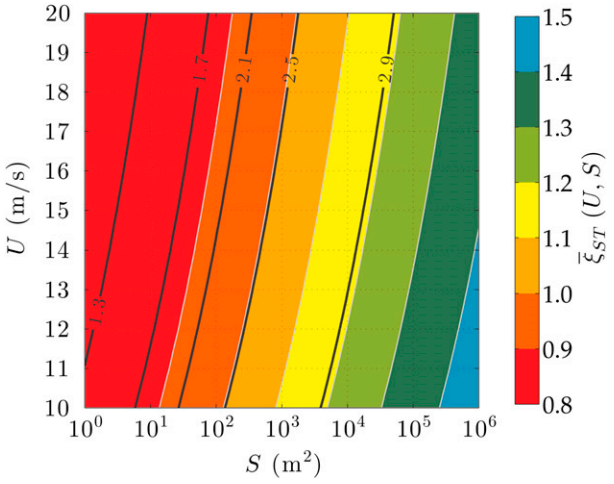

FIG. 1. Dimensionless space–time extremes $\bar{\xi}_{ST}$ for PM+cos^2 directional spectrum, as a function of wind speed U and space domain size S. Time domain size is $T = 100\tau$. Black solid lines represent wave dimension β.

20% of the total variation observed. In fetch-limited seas (Fig. 2), $\bar{\xi}_{ST}(U, F, S)$ ranges from 0.8 to 1.7, growing for increasing S and reducing for increasing U and F. In this context, F has a stronger effect than U. Indeed, a $\bar{\xi}_{ST}(U, F, S)$ variation equal to the 30% of the total at most is found modifying F from 1 to 250 km, whereas a variation of 10% at most is found modifying U from 10 to 20 m s^{-1}. As for $\bar{\xi}_{ST}(U, S)$, the dependence of $\bar{\xi}_{ST}(U, F, S)$ upon S seems to be much more effective than those upon U and F. Comparing the bottom-right panel of Fig. 2 to Fig. 1 reveals that at $F = 250$ km, the sea states, especially those with the smallest U, are close to the transition to fully developed condition.

As shown in Figs. 1 and 2, the wave dimension β is mostly affected by S, approaching 1 for the smallest S and 3 for the largest areas. Conversely, β is weakly modified by U and F. Actually, β and $\bar{\xi}_{ST}$ levels are almost equidistant, revealing a common behavior with respect to S. Most likely, this is because of the average number of waves M_3, M_2, and M_1 but particularly M_3. Indeed over a ST domain, as shown in Eqs. (6) and (7), $\bar{\xi}_{ST}$ and β are principally governed by M_3; the more M_3 is large, the more $\bar{\xi}_{ST}$ grows and β tends to 3. This condition can be achieved by increasing $S = XY$ for a given sea state or by reducing τ, L_x, and L_y and increasing α_{xt}, α_{xy}, and α_{yt} for a given S.

The dependence of the spectral parameters upon U and F, expressed through Eqs. (19) and (27), is displayed in Fig. 3 for fully developed sea states, as a function of U, and for fetch-limited sea states, as a function of the dimensionless fetch $F^* = Fg/U^2$ and in terms of the dimensionless spectral parameters $\tau^* = \tau g/U$ and $L_i^* = L_i g/U^2$ ($i = x, y$). In fully developed conditions, τ, L_x, and L_y increase with U. The ratio L_x/L_y, that is, the short crestedness of the sea state, remains constant ($\gamma_s \approx 0.58$) because the directional distribution of variance is not modified by wind in the analysis. Because of this, the irregularity parameters remain null, except α_{xt}, which slightly decreases with U, meaning that the sea state tends to be slightly more confused. Actually, the dependence of α_{xt} upon U appears to be weak, and hence for the reasons explained above τ, L_x, and L_y act as the driving factors for the reduction of $\bar{\xi}_{ST}$ shown in Fig. 1. Parameters τ, L_x, and L_y increase in fetch-limited conditions too; for smaller F^* the increase is rapid, while for larger F^* the increase is slower, and parameters appear to tend to the fully developed condition values. The short crestedness is conserved in the analysis, while the ST randomness of the sea state, expressed by the irregularity parameters, slightly changes according to the change of α_{xt}. This rapidly decreases within the smallest F^* range and then settles on a value approximately constant over F^*. Thus, also in fetch-limited conditions, the reduction of $\bar{\xi}_{ST}$ shown in Fig. 2 is mainly driven by the growth of τ, L_x, and L_y.

Wind speed U and fetch F have shown considerable effects on the spectral parameters, particularly on the geometric parameters τ, L_x, and L_y. Indeed, in fully developed conditions, U forces them to increase until they doubled (τ) and almost tripled (L_x and L_y) at 20 m s^{-1} with respect to the 10 m s^{-1} values. This has generally a direct effect on the average numbers of waves, and thus one could expect a direct effect on the ST extremes too. Nevertheless, the corresponding $\bar{\xi}_{ST}$ variation due to U is very weak compared to that of the spectral parameters, being at 20 m s^{-1} only 18% of the 10 m s^{-1} value. Similar considerations can be drawn for fetch-limited sea states. From the analysis, it emerges that the spectral parameters variations are damped out in Eq. (6), which leads to ST extreme estimates that are only slightly sensitive to variations in the number of waves, as noted by Holthuijsen (2007) for a time domain extreme statistics.

The cos^2 function employed in this study provided a reasonable though simplified representation of the directional distribution in short-crested seas (Holthuijsen 2007). Indeed, it is unimodal and frequency independent, whereas realistic sea states have been proven to be bimodal (for $\sigma > \sigma_p$) and frequency dependent in the distribution of energy (Ewans 1998). To evaluate the error ascribable to the use of a constant spreading distribution in fetch-limited seas, we tested the use of a distribution which models a frequency-dependent spreading. To this end, we considered the cos2s directional distribution function with the parameterization proposed by Ewans (1998) for the spreading parameter s. Hence, the directional spreading (which is

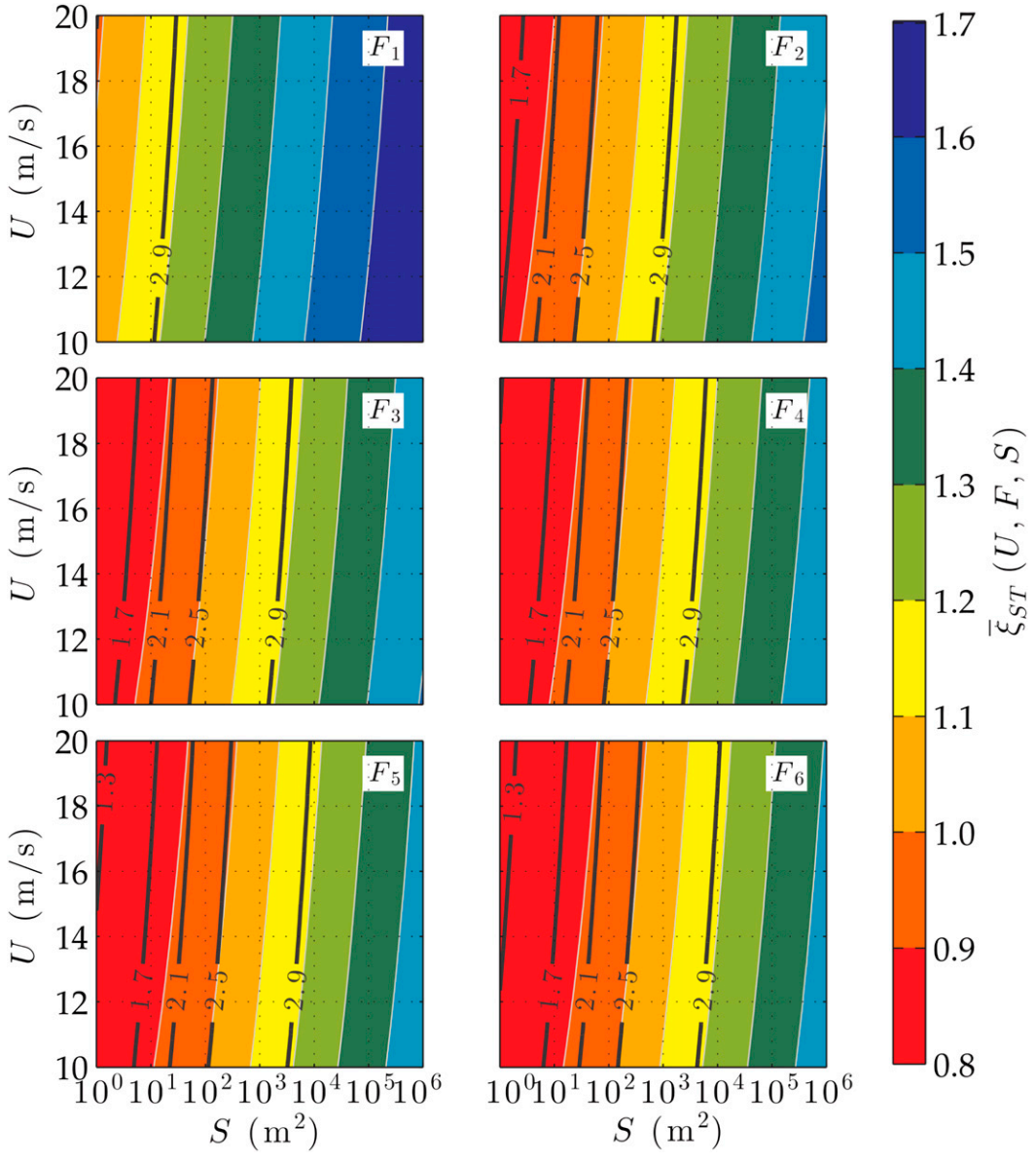

FIG. 2. Dimensionless space–time extremes $\overline{\xi}_{ST}$ for JON+cos^2 directional spectrum, as a function of wind speed U and space domain size S, for six different fetches: $F_1 = 1$ km, $F_2 = 50$ km, $F_3 = 100$ km, $F_4 = 150$ km, $F_5 = 200$ km, and $F_6 = 250$ km. Time domain size is $T = 100\tau$. Black solid lines represent wave dimension β.

minimum at the peak frequency) increased both toward larger and smaller frequencies, in agreement with observations of directional spectra at sea. In this context, we compared the spectral parameters and the $\overline{\xi}_{ST}$ predictions of FM obtained from two directional spectra sharing the same frequency part (i.e., JON with $A_{JON} = 0.014$, $\sigma_p = 1.2\,\text{rad}\,\text{s}^{-1}$, $\gamma = 2.0$, and $\phi = 0.08$) but having different directional distribution: a JON+cos^2 and a JON+cos2s, assuming the latter as the reference. Spectral parameters were obtained by means of the numerical integration of the spectra, whose frequency-direction domain was discretized as in section 5. We tested a wide range of S (from 1 to $10^6\,\text{m}^2$), observing significant differences in the spectral parameters L_x (14%), L_y (−23%), and α_{xt} (−7%). Nevertheless, such variations, though considerable, are not responsible for similar changes in the ST extremes, as previously shown in this section. Indeed, the $\overline{\xi}_{ST}$ obtained with the simplified cos^2 distribution are only 1% smaller than those obtained with the more realistic cos2s distribution. As an additional verification, we also compared the ST extremes computed from a JON+cos^2 spectrum with the extremes

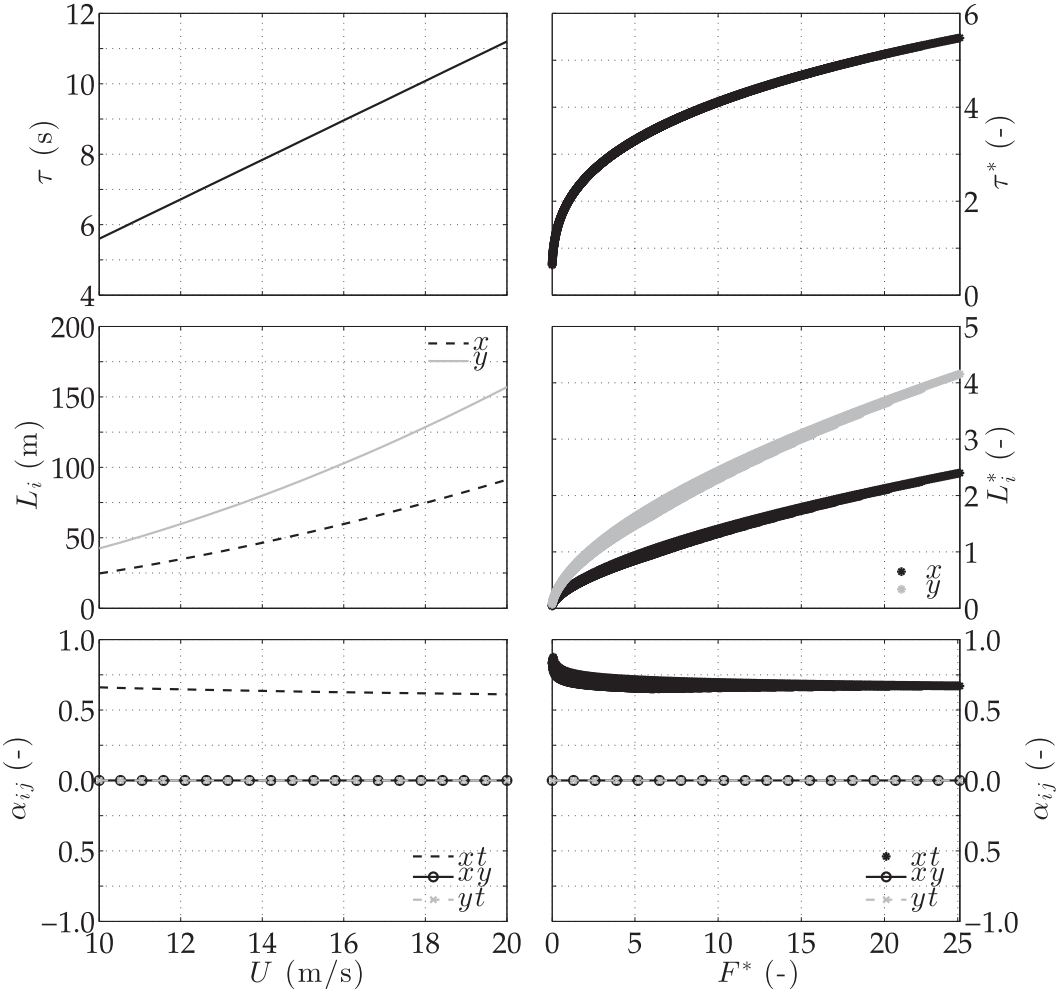

FIG. 3. Spectral parameters for (left) PM+cos^2 and (right) JON+cos^2 directional spectra. For JON+cos^2, dimensionless parameters are plotted.

retrieved from numerical simulations of Gaussian JON+cos2s sea states. To this aim, a set of 100 realizations $\eta(x, y, t)$ of a JON+cos2s sea state was generated using WAFO (using the same domain discretization and JON spectrum of section 5), and the expected ST extremes detected over five ST volumes with the same duration ($T = 1$ hour) and different areas ($S_j = j^2 L_x L_y$ with $j = 1, 2, 3, 4, 5$, $L_x \approx 16$ m, and $L_y \approx 19$ m) were compared to the FM predictions of a JON+cos^2 sea state sharing the JON spectrum. Such predictions, though obtained by means of a simplified directional distribution function, are in agreement with the simulations within a 1% error.

b. *Current- and depth-induced shoaling effects*

We investigated the effects of current- and depth-induced shoalings on ST extremes by means of the SWAN-ST implementation. To analyze the contributions of complex processes (e.g., wave–current interactions) separately, in this paper we focused on the shoaling effect only, thus neglecting, for instance, the refractive phenomena induced by different wave–current directions and planimetric bottom variations. Shoaling is completely modeled within the propagative terms in the left-hand side of Eq. (28), and it could be altered by dissipative phenomena [e.g., wave breaking or bottom friction (Holthuijsen 2007)], and hence no source term was accounted for in Eq. (28). We performed stationary model runs over a 1D domain, imposing (at the deep-water boundary) the propagation of a PM+cos^2 over an ambient current or over a sloping bottom, and we simulated the spectral parameters at each grid node of the model domain. The model setup used has already been described in section 4. We tested four different sea states with $H_{s,0} =$ 1.0, 2.0, 4.0, and 8.0 m (subscript 0 referring to still or deep water conditions), and we computed the extremes over ST

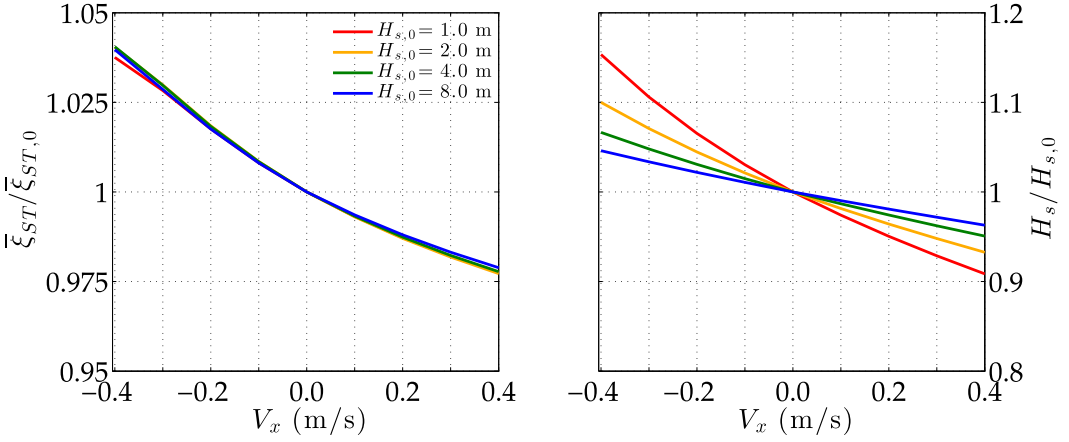

FIG. 4. Current-induced shoaling effects on (left) space–time extremes $\overline{\xi}_{ST}$ and (right) significant wave height H_s. Subscript 0 refers to still water conditions, that is, $V_x = 0\,\mathrm{m\,s^{-1}}$. Time domain size is $T = 100\tau$; space domain size is $S = XY = \overline{L}_{x,0}\overline{L}_{y,0}$.

domains centered on the grid nodes. Since we already discussed the effect on $\overline{\xi}_{ST}$ of the space domain size S, herein the ST domain size for each sea state tested was fixed (i.e., $S = XY = L_{x,0}L_{y,0}$ and $T = 100\tau_0$). Unlike the analytical analysis of section 6a, using a numerical model we did not impose any constraint to the directional distribution function that was free to evolve under the different forcings effect, starting from an initial common spectral shape.

1) CURRENT-INDUCED SHOALING

Current-induced shoaling effects were investigated by imposing the transition from the propagation over still waters (i.e., current speed $V_x = 0\,\mathrm{m\,s^{-1}}$ in the first half of the domain) to the propagation over a moving medium (i.e., $V_x \neq 0$ in the last half of the domain). Eight different current speeds were tested, that is, -0.4, -0.3, -0.2, -0.1, 0.1, 0.2, 0.3, and $0.4\,\mathrm{m\,s^{-1}}$, limiting the analysis to $-0.4\,\mathrm{m\,s^{-1}}$, which is the critical speed $V_{x,c} = -c/4$ over which the highest harmonic of the spectrum (i.e., with 1.0-Hz relative frequency and phase speed $c = 1.56\,\mathrm{m\,s^{-1}}$) is affected by energy blocking and energy reflection phenomena (Phillips 1977). The tail contribution to the spectral moments was not accounted for in this specific analysis because we could not control how the spectrum is modified by the current effect outside the prognostic frequency range.

Prior to studying the effect of current-induced shoaling on ST extremes, we analyzed the effects on H_s (Fig. 4); it increases in upcurrent conditions (15% at most, at $-0.4\,\mathrm{m\,s^{-1}}$), and it decreases in downcurrent conditions (9% at most, at $0.4\,\mathrm{m\,s^{-1}}$), in agreement with current-induced shoaling (Holthuijsen 2007). Moreover, the higher H_s in still waters, the smaller the modifications under the current effect. A similar effect on ST extremes is depicted in Fig. 4; $\overline{\xi}_{ST}$ increases upcurrent (4% at most) and decreases downcurrent (2% at most). The trends shown suggest that such variations should be even larger in the presence of stronger currents. Under the effect of a current, sea states with different $H_{s,0}$ show comparable variations of $\overline{\xi}_{ST}$ (at $-0.4\,\mathrm{m\,s^{-1}}$, the range of variations relative to the maximum is less than 1%), although the range of variations of the spectral parameters and H_s is larger, especially on an opposite current (at $-0.4\,\mathrm{m\,s^{-1}}$, the range of variations relative to the maximum is up to 10%). This is a consequence of $\overline{\xi}_{ST}$ being normalized by H_s and not much sensitive to the number of waves' variations. Results also indicate that the dimensional ST extremes, $\overline{\eta}_{ST} = \overline{\xi}_{ST}H_s$, are magnified over an opposite current by the increase of H_s and $\overline{\xi}_{ST}$. While the H_s increase has been already motivated, the $\overline{\xi}_{ST}$ increase can be explained by an increase in the number of waves (i.e., M_3, M_2, and M_1), which is in turn caused by a decrease of the spectral parameters. This is confirmed by the results shown in Fig. 5, where τ, L_x, L_y, and α_{xt} decrease on an opposite current (α_{yt} and α_{xy} variations are negligible, and hence they are not plotted), indicating an average shortening of waves in time (16% at most on τ) and space (40% at most on L_x). The decrease of τ is in agreement with the frequency downshifting typical of shoaling (Holthuijsen 2007), and the decrease of L_x is consistent with the kinematics of waves on a moving medium (Phillips 1977). Also, L_y shorten on average (8% at most) and since L_x variation is considerably larger than L_y variation, then waves appear longer crested ($\gamma_s < \gamma_{s,0}$). In addition, the sea state tends to be more confused, as indicated by the decrease of α_{xt} (10% at most). Instead, on a following current, τ, L_x, L_y, and α_{xt} increase (Fig. 5), causing the average number of waves to reduce and in turn causing $\overline{\xi}_{ST}$ to decrease. Apart from L_x, whose

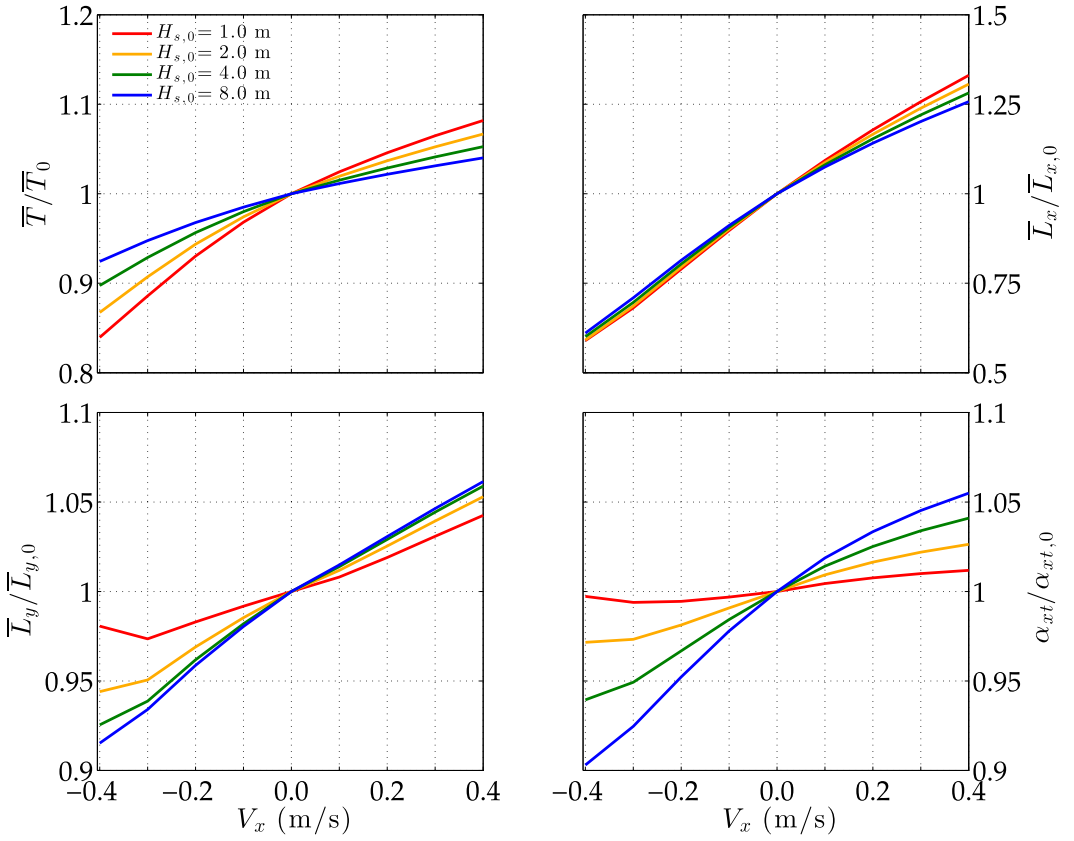

FIG. 5. Current-induced shoaling effects on spectral parameters (except α_{xy} and α_{yt} whose variations can be neglected). Subscript 0 refers to still water conditions, that is, $V_x = 0\,\mathrm{m\,s^{-1}}$.

variation is comparable to the upcurrent decrease, the increase of the other spectral parameters is (at most) halved with respect to the decrease shown with opposite current. Moreover, waves on the following current are more short crested than in still waters (viz., $\gamma_s < \gamma_{s,0}$), though more organized (viz., $\alpha_{xt} > \alpha_{xt,0}$).

2) DEPTH-INDUCED SHOALING

Depth-induced shoaling effects on spectral parameters and ST extremes were investigated by imposing the wave propagation over a sloping bottom whose depth, starting from a deep-water condition (i.e., 350 m), decreased to a minimum depth. The minimum depths, ranging from 2 to 125 m depending on the test, were chosen in order to observe the shoaling process in all the spectral components of the tested spectra.

As a first step, we analyzed the H_s variation toward the shallow depths. In Fig. 6, H_s initially decreases below the deep-water value and then grows above it consistently with the antibunching and bunching of energy peculiar of shoaling (Holthuijsen 2007). It is noteworthy that in the shallowest part, the remarkable H_s growth (up to almost 40% of $H_{s,0}$) should be realistically limited by shallow-water dissipation processes such as bottom friction and depth-induced breaking. The variation of $\overline{\xi}_{\mathrm{ST}}$ with bottom depth is somehow reversed with respected to that of H_s (Fig. 6). Indeed, $\overline{\xi}_{\mathrm{ST}}$ slightly increases over the deepest bottoms and then drops toward the shallowest, counteracting the H_s reduction and increment, respectively. Nevertheless, modifications induced by depth-induced shoaling on $\overline{\xi}_{\mathrm{ST}}$ are significantly weaker than those induced on H_s, and as a consequence, dimensional maxima, $\overline{\eta}_{\mathrm{ST}} = \overline{\xi}_{\mathrm{ST}} H_s$, vary according to H_s. All the sea states tested show similar tendencies, and as for current-induced shoaling, the variations experienced by the spectral parameters and H_s for different $H_{s,0}$ are largely reduced for $\overline{\xi}_{\mathrm{ST}}$, whose variations in the presence of different $H_{s,0}$ are significantly reduced due to normalization and due to the slight sensitivity of $\overline{\xi}_{\mathrm{ST}}$ to the number of waves' variation. The growth and decay of $\overline{\xi}_{\mathrm{ST}}$ can be motivated by the spectral parameters' variations under the depth-induced shoaling effect, illustrated in Fig. 7 (α_{yt} and α_{xy} remain null). Indeed, approaching the shallow waters, at first τ decreases (up to 5% of the deep-water value τ_0) and then increases (up to 15% of τ_0) because of the spectral frequency shifting

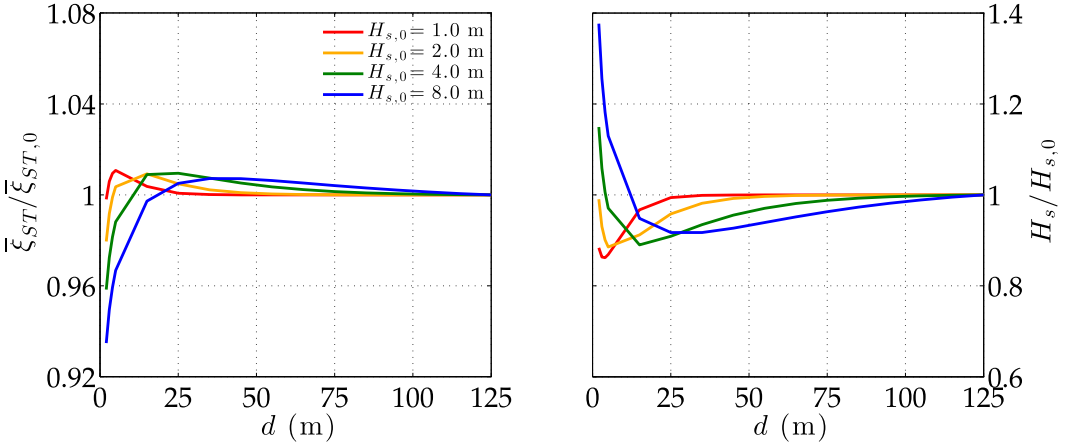

FIG. 6. Depth-induced shoaling effects on (left) space–time extremes $\overline{\xi}_{ST}$ and (right) significant wave height H_s. Subscript 0 refers to deep-water conditions. Time domain size is $T = 100\,\tau_0$; space domain size is $S = XY = \overline{L}_{x,0}\overline{L}_{x,0}$.

typical of shoaling: upshifting over the largest depths and downshifting over the smallest depths (Holthuijsen 2007). Parameter L_x monotonically decreases (40% of $L_{x,0}$ at most) from deep to shallow waters due to the phase speed slow down, whereas L_y shows an initial slight decrease followed by an increase (80% of $\overline{L}_{y,0}$ at most). It follows that $\gamma_s \ll \gamma_{s,0}$, and hence waves in shallow waters appear much more long crested than in deep waters. At the same time the sea state is more organized, with α_{xt} larger than in deep waters.

7. Conclusions

In this paper, we presented an analytical and numerical study aimed at discussing the influence of metocean forcings on the space–time extremes of short-crested sea states. In particular, the roles of the wind conditions and wave interaction with an ocean current and with the bottom were investigated by analyzing the effects on the space–time integral parameters of the directional spectrum. Space–time extreme $\overline{\xi}_{\mathrm{ST}}$ estimates were based upon the Fedele model, whose performance was assessed by comparing the theoretical predictions to the expected values from numerical simulations of Gaussian sea states, showing an excellent agreement.

To investigate the wind conditions effect, we attained two sets of formulations for deep waters' fully developed (Pierson–Moskowitz) and fetch-limited (JONSWAP) sea states to express the dependence of spectral parameters upon the wind speed and fetch. We pointed out that such formulations depend upon a cutoff frequency σ_c (imposed to ensure the boundedness of the higher-order moments) and upon the power m of the $\cos^m$ directional distribution function (herein $m = 2$). The cutoff frequency was influential on the spectral parameters but significantly less relevant for space–time extremes computation. In the future, the procedure herein used could be generalized to attain more general formulations that depend upon arbitrary cutoff frequency and directional spreading. Nevertheless, we assessed that the $\overline{\xi}_{\mathrm{ST}}$ estimate obtained using the $\cos^2$ directional distribution almost matches that one obtained using a more realistic directional distribution (with frequency-dependent spreading).

To investigate the effects of current- and depth-induced shoaling, we adapted the SWAN numerical wave model in order to store the relevant integrated spectral parameters at the nodes of the computational grid, as a resources-saving alternative to the storage of the spectra. Running a 1D model we found that the diagnostic spectral tail adds a small contribution to the space–time extremes, which could be neglected when the tail parameterization is not given for sure. In the future, the effects of wave steepness, which may be not negligible in the presence of strong opposing currents or approaching the shore, as well as the effects of bottom friction should be studied in the context of a higher-order wave model, and depth-induced breaking should be explored.

The main results presented in the paper are summarized as follows:

- Compared to the significant wave height H_s, the increasing wind conditions turned out to have a weakening effect on the space–time extremes (both in fully developed and fetch-limited conditions). Indeed, we generally observed a reduction of $\overline{\xi}_{\mathrm{ST}}$ increasing the wind speed and the fetch (for a given space domain size S) as a consequence of the spectral parameters' variations inside the space–time domain. Hence, the

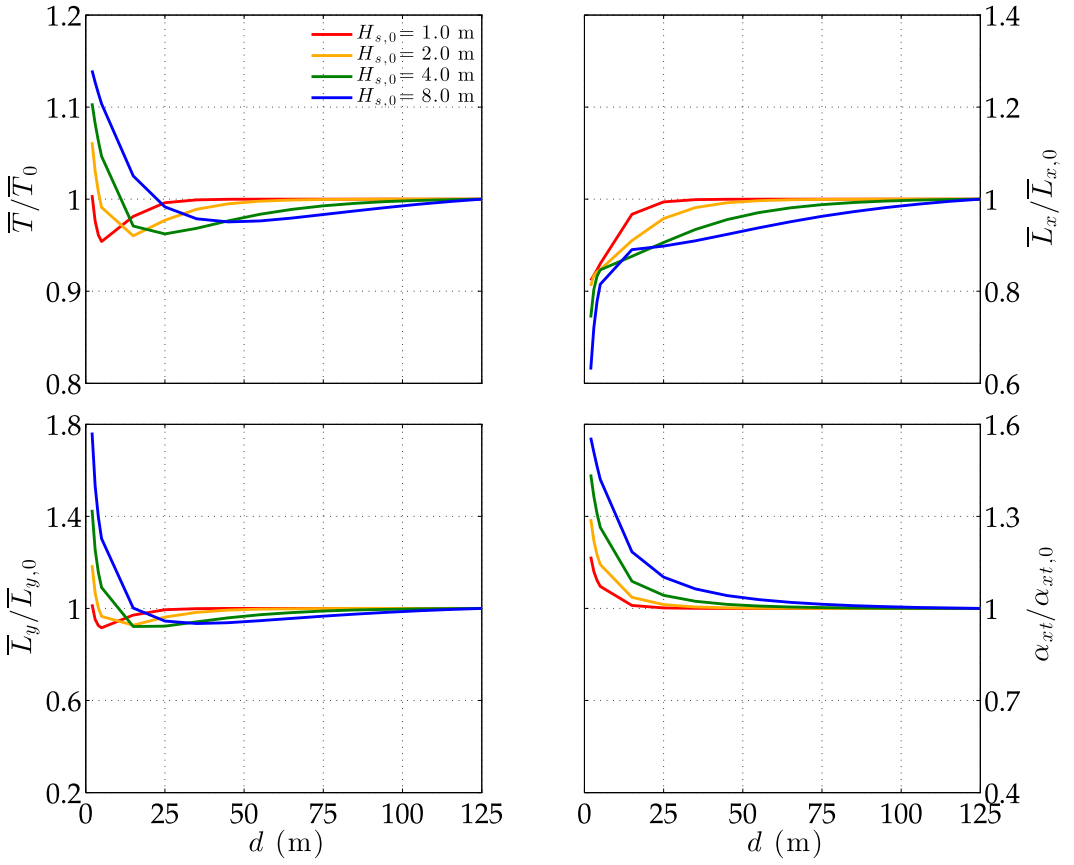

FIG. 7. Depth-induced shoaling effects on spectral parameters (except α_{xy} and α_{yt} whose variations can be neglected). Subscript 0 refers to deep-water conditions.

wind effect on the dimensional extremes $\overline{\eta}_{ST} = \overline{\xi}_{ST} H_s$ is to reduce the increment expected in presence of more severe wind conditions. As a matter of fact, the reduction of $\overline{\xi}_{ST}$ counteracts the increase of H_s, thus reducing the increment of $\overline{\eta}_{ST}$.

- The current-induced shoaling was found to amplify the space–time extremes in the presence of opposite currents and to reduce them in presence of following currents (for given S and H_s) as a result of the spectral parameters modifications. Therefore, the upcurrent effect on $\overline{\eta}_{ST}$ is to further increase the increment expected due to the H_s contribution, and the downcurrent effect is to intensify the expected reduction.
- The depth-induced shoaling exerted a weakening effect on the space–time extremes, since we observed a $\overline{\xi}_{ST}$ reduction in the shallow depths caused by the spectral parameters variations. Such reduction counteracted the typical depth-induced increase of H_s toward the shore, thus reducing the increment of $\overline{\eta}_{ST}$ expected in shallow waters.
- The space domain size S had a strong influence on the space–time extremes, as expected. Indeed, a significant increase of $\overline{\xi}_{ST}$ was obtained enlarging S for a given sea state, providing evidence to support the role of the space domain size S in the prediction of extremes at sea.

Acknowledgments. The research was supported by the Flagship Project RITMARE—The Italian Research for the Sea coordinated by the Italian National Research Council and funded by the Italian Ministry of Education, University and Research within the National Research Program 2011–2013. The authors gratefully acknowledge Prof. Francesco Fedele from GeorgiaTech (Atlanta, Georgia, United States) for useful comments. The SWAN model (version 40.85) was modified under the terms of the GNU General Public License.

REFERENCES

Abramowitz, M., and I. A. Stegun, Eds., 1965: *Handbook of Mathematical Functions with Formulas, Graphs, and Mathematical Tables.* National Bureau of Standards Applied Mathematics Series, Vol. 55, Dover, 1046 pp.

Adler, R. J., 1981: *The Geometry of Random Fields.* John Wiley & Sons, 280 pp.

——, and J. E. Taylor, 2007: *Random Fields and Geometry, Springer Monogr. Math.,* Vol. 115, Springer, 448 pp.

Banner, M., J. Trinder, and I. Jones, 1989: Wavenumber spectra of short gravity waves. *J. Fluid Mech.,* **198,** 321–344, doi:10.1017/S0022112089000157.

Barbariol, F., A. Benetazzo, F. Bergamasco, S. Carniel, and M. Sclavo, 2014: Stochastic space-time extremes of wind sea states: Validation and modeling. *Proc. ASME 2014 33rd Int. Conf. on Ocean, Offshore and Arctic Engineering,* San Francisco, CA, ASME, 11 pp., doi:10.1115/OMAE2014-23997.

Baxevani, A., and I. Rychlik, 2006: Maxima for Gaussian seas. *Ocean Eng.,* **33,** 895–911, doi:10.1016/j.oceaneng.2005.06.006.

——, K. Podgórski, and I. Rychlik, 2003: Velocities for moving random surfaces. *Probab. Eng. Mech.,* **18,** 251–271, doi:10.1016/S0266-8920(03)00029-8.

Benetazzo, A., 2006: Measurements of short water waves using stereo matched image sequences. *Coastal Eng.,* **53,** 1013–1032, doi:10.1016/j.coastaleng.2006.06.012.

——, F. Fedele, G. Gallego, P. Shih, and A. Yezzi, 2012: Offshore stereo measurements of gravity waves. *Coastal Eng.,* **64,** 127–138, doi:10.1016/j.coastaleng.2012.01.007.

Boccotti, P., 2000: *Wave Mechanics for Ocean Engineering.* Vol. 64, Elsevier Oceanography Series, Elsevier, 496 pp.

Booij, N., R. Ris, and L. Holthuijsen, 1999: A third-generation wave model for coastal regions. I: Model description and validation. *J. Geophys. Res.,* **104,** 7649–7666, doi:10.1029/98JC02622.

Cavaleri, L., L. Bertotti, L. Torrisi, E. Bitner-Gregersen, M. Serio, and M. Onorato, 2012: Rogue waves in crossing seas: The Louis Majesty accident. *J. Geophys. Res.,* **117,** C00J10, doi:10.1029/2012JC007923.

Dankert, H., J. Horstmann, S. Lehner, and W. Rosenthal, 2003: Detection of wave groups in SAR images and radar image sequences. *IEEE Trans. Geosci. Remote Sens.,* **41,** 1437–1446, doi:10.1109/TGRS.2003.811815.

Dysthe, K., H. E. Krogstad, and P. Müller, 2008: Oceanic rogue waves. *Annu. Rev. Fluid Mech.,* **40,** 287–310, doi:10.1146/annurev.fluid.40.111406.102203.

Ewans, K. C., 1998: Observations of the directional spectrum of fetch-limited waves. *J. Phys. Oceanogr.,* **28,** 495–512, doi:10.1175/1520-0485(1998)028<0495:OOTDSO>2.0.CO;2.

Fedele, F., 2012: Space–time extremes in short-crested storm seas. *J. Phys. Oceanogr.,* **42,** 1601–1615, doi:10.1175/JPO-D-11-0179.1.

——, A. Benetazzo, G. Gallego, P.-C. Shih, A. Yezzi, F. Barbariol, and F. Ardhuin, 2013: Space-time measurements of oceanic sea states. *Ocean Modell.,* **70,** 103–115, doi:10.1016/j.ocemod.2013.01.001.

Forristall, G. Z., 1981: Measurements of a saturated range in ocean wave spectra. *J. Geophys. Res.,* **86,** 8075–8084, doi:10.1029/JC086iC09p08075.

——, 2005: Understanding rogue waves: Are new physics really necessary. *Rogue Waves: 'Aha Huliko'a Hawaiian Winter Workshop,* Honolulu, HI, University of Hawai'i at Mānoa, 29–35. [Available online at http://www.soest.hawaii.edu/PubServices/2005pdfs/Forristall.pdf.]

——, 2006: Maximum crest wave heights over an area and the air gap problem. *Proc. 25th Int. Conf. on Offshore Mechanics and Arctic Engineering,* Hamburg, Germany, ASME, 11–15, doi:10.1115/OMAE2006-92022.

——, 2007: Wave crest heights and deck damage in Hurricanes Ivan, Katrina, and Rita. *Offshore Technology Conf.,* Houston, TX, Offshore Technology Conference, OTC-18620-MS, doi:10.4043/18620-MS.

——, 2011: Maximum crest heights under a model TLP deck. *Proc. ASME 2011 30th Int. Conf. on Ocean, Offshore and Arctic Engineering,* Rotterdam, Netherlands, ASME, 571–577, doi:10.1115/OMAE2011-49837.

Gemmrich, J., and C. Garrett, 2008: Unexpected waves. *J. Phys. Oceanogr.,* **38,** 2330–2336, doi:10.1175/2008JPO3960.1.

Gran, S., 1992: *A Course in Ocean Engineering.* Developments in Marine Technology Series, Vol. 8, Elsevier, 583 pp.

Günther, H., S. Hasselmann, and P. A. Janssen, 1992: *The WAM Model: Cycle 4.* DKRZ, 91 pp.

Hasselmann, K., and Coauthors, 1973: *Measurements of Wind-Wave Growth and Swell Decay during the Joint North Sea Wave Project (JONSWAP).* Deutsche Hydrographisches Institut, 95 pp.

Hasselmann, S., and Coauthors, 1988: The WAM model—A third generation ocean wave prediction model. *J. Phys. Oceanogr.,* **18,** 1775–1810, doi:10.1175/1520-0485(1988)018<1775:TWMTGO>2.0.CO;2.

Holthuijsen, L. H., 2007: *Waves in Oceanic and Coastal Waters.* Cambridge University Press, 387 pp.

Kitaigorodskii, S., 1962: Applications of the theory of similarity to the analysis of wind-generated wave motion as a stochastic process. *Izv. Geophys. Ser. Acad. Sci., USSR,* **1,** 105–117.

Krogstad, H. E., J. Liu, H. Socquet-Juglard, K. B. Dysthe, and K. Trulsen, 2004: Spatial extreme value analysis of nonlinear simulations of random surface waves. *Proc. ASME 23rd Int. Conf. on Offshore Mechanics and Arctic Engineering,* Vancouver, BC, Canada, ASME, 285–295, doi:10.1115/OMAE2004-51336.

Lewis, A., and R. Allos, 1990: JONSWAP's parameters: Sorting out the inconsistencies. *Ocean Eng.,* **17,** 409–415, doi:10.1016/0029-8018(90)90032-2.

Ochi, M., 2005: *Ocean Waves: The Stochastic Approach.* Cambridge Ocean Technology Series, Vol. 6, Cambridge University Press, 332 pp.

Phillips, O. M., 1977: *The Dynamics of the Upper Ocean.* Cambridge University Press, 336 pp.

Pierson, J. W. J., and L. Moskowitz, 1964: A proposed spectral form for fully developed wind seas based on the similarity theory of S.A. Kitaigorodskii. *J. Geophys. Res.,* **69,** 5181–5190, doi:10.1029/JZ069i024p05181.

Piterbarg, V. I., 1996: *Asymptotic Methods in the Theory of Gaussian Processes and Fields. Transl. Math. Monogr.,* Vol. 148, 206 pp.

Rosenthal, W., and S. Lehner, 2008: Rogue waves: Results of the MaxWave project. *J. Offshore Mech. Arct. Eng.,* **130,** 021006, doi:10.1115/1.2918126.

Sand, S. E., N. O. Hansen, P. Klinting, O. T. Gudmestad, and M. J. Sterndorff, 1990: Freak wave kinematics. *Water Wave Kinematics,* Springer, 535–549.

Shemdin, O. H., H. M. Tran, and S. Wu, 1988: Directional measurement of short ocean waves with stereophotography. *J. Geophys. Res.,* **93,** 13 891–13 901, doi:10.1029/JC093iC11p13891.

Skourup, J., N.-E. O. Hansen, and K. Andreasen, 1997: Non-Gaussian extreme waves in the central North Sea. *J. Offshore Mech. Arct. Eng.,* **119,** 146–150, doi:10.1115/1.2829061

Socquet-Juglard, H., 2005: Spectral evolution and probability distributions of surface ocean gravity waves and extreme waves. D.Sc. thesis, University of Bergen, 71 pp.

——, K. Dysthe, K. Trulsen, H. E. Krogstad, and J. Liu, 2005: Probability distributions of surface gravity waves during

spectral changes. *J. Fluid Mech.,* **542,** 195–216, doi:10.1017/S0022112005006312.

SWAN Team, 2011: SWAN cycle III, version 40.85: Scientific and technical documentation. Delft University of Technology, accessed 4 June 2015. [Available online at swanmodel.sourceforge.net.]

WAFO Group, 2011: WAFO—A MATLAB toolbox for analysis of random waves and loads: Tutorial for WAFO version 2.5. Centre for Mathematical Statistics, Lund University Rep., 185 pp. [Available online at www.maths.lth.se/matstat/wafo/documentation/wafotutor25.pdf.]

Yamaguchi, M., 1984: Approximate expressions for integral properties of the JONSWAP spectrum. *Proc. Japan. Soc. Civ. Eng.,* **345,** 149–152.

Young, I. R., 1999: *Wind Generated Ocean Waves.* Elsevier Ocean Engineering Series, Vol. 2, Elsevier, 288 pp.